A prenatal window for enhancing spatial resolution of cortical barrel maps

Mar Aníbal-Martínez[1], Lorenzo Puche-Aroca[1], Gabriele Pumo[2,3], M. Pilar Madrigal[4], Luis M. Rodríguez-Malmierca[1], Francisco J. Martini[1], Filippo M. Rijli[2,3], Guillermina López-Bendito[1,*]

[1]Instituto de Neurociencias de Alicante, Universidad Miguel Hernández-Consejo Superior de Investigaciones Científicas (UMH-CSIC), San Juan de Alicante, Alicante, Spain.

[2] Friedrich Miescher Institute for Biomedical Research, Maulbeerstrasse 66, 4058 Basel, Switzerland.

[3]University of Basel, Basel, Switzerland.

[4]Departamento de Histología y Anatomía, Facultad de Medicina, Universidad Miguel Hernández (UMH), San Juan de Alicante, Alicante, Spain.

*Correspondence: g.lbendito@umh.es (G.L-B)

Keywords: sensory cortex, specification, barrel field, development, thalamus, calcium waves, whiskers, mouse

ABSTRACT

Precise mapping of peripheral inputs onto cortical areas is required for appropriate sensory processing. In the mouse primary somatosensory cortex, mystacial whiskers are represented in large barrels, while upper lip whiskers are in smaller, less defined barrels. Barrel size and definition of these two functionally distinct barrel maps are believed to be determined by the type of whisker input and peripheral receptor density. However, spontaneous activity and transcriptional programs at prenatal developmental stages can influence somatosensory map development independently of sensory experience. Thus, the mechanisms defining distinct barrel field territories, including their size and definition, remain poorly understood. Here, we show that prenatal ablation of mystacial whiskers remap somatosensory cortical territories resulting in enhancement of the functional and anatomical definition of upper lip whisker barrels. These changes do not result from alterations in receptor type but rather stem from thalamic upper lip input-receiving neurons adopting a mystacial-like transcriptional profile. Our results unveil a regulated prenatal mechanism within the thalamus that maps available somatosensory input to ensure sufficient cortical barrel size and functional spatial resolution for sensory processing, irrespective of peripheral receptor type and density.

INTRODUCTION

Sensory systems are represented in the primary sensory areas of the brain, structured into both anatomical and functional maps[1-4]. The spatial precision of sensory maps varies among species according to the ethological relevance of the modality or the intra-modal sensory branch[5]. This precision is achieved through the accuracy of point-to-point innervation along the ascending sensory pathway. In rodents, which heavily rely on the somatosensory modality, a prominent cortical area is devoted to processing stimuli from facial whiskers. Within the mouse primary somatosensory cortex (S1), information from facial whiskers is processed in two juxtaposed subfields: the postero-medial barrel subfield (PMBSF) and the antero-lateral barrel subfield (ALBSF). The PMBSF receives input from the mystacial whiskers which provide diverse and specialized information to S1[6,7]. The ALBSF receives input from the upper lip whiskers which are considered to play a secondary role in sensory processing[8]. While each barrel corresponds to a single whisker in both regions, the degree of clustering of incoming thalamocortical axons varies, leading to notable anatomical distinctions between the two territories. While PMBSF barrels are characterized by their large size and sharp borders, ALBSF barrels are smaller and have poorly defined borders[9]. These differences in intra-modal map organization parallel the distinct morphological characteristics of mystacial and upper lip whiskers: mystacial whiskers are long with large follicles, whereas upper lip whiskers are comparatively short with small follicles, albeit more abundant. Despite their clear anatomical and functional differences, we still lack a complete understanding of the mechanism underlying the construction of these two distinct barrel maps and to what extent they rely on the type of sensory receptors (mystacial versus upper lip). Indeed, recent data demonstrated that sensory receptor-independent mechanisms can also influence cortical barrel size by altering the patterns of activity in subcortical stations. For instance, increasing thalamic waves in the developing somatosensory thalamus of early blind mice results in larger barrels in the PMBSF of S1, even before the onset of active whisking[10,11]. Thus, the size of a sensory barrel map may not only depend on the type

and number of sensory receptors but may also be regulated by intrinsic programs during development. By embryonically ablating mystacial whiskers and follicles, and the subsequent PMBSF representation, we generated mice in which the ALBSF barrels become larger and better-defined, without altering the size and number of upper lip follicles. This reorganization of the barrel maps occurs within a restricted prenatal time window and is guided by transcriptional programs operating intra-modally in the thalamus. Interestingly, these reorganized ALBSF barrels resemble normal PMBSF barrels at the morphological, molecular and functional levels, showing an enhanced spatial resolution upon tactile stimulation.

RESULTS

The size of barrel subfield areas can be adjusted prenatally

The size of the areas devoted to processing distinct whisker -mystacial versus upper lip-input information is thought to be determined by the corresponding type and density of sensory receptors on the mouse face[12,13]. We asked whether prenatal removal of a selected facial whisker type might have an impact on the cortical barrel areas and spatial distribution of the spared whiskers. We implemented a strategy whereby the mystacial whiskers in the whisker pad were cauterized unilaterally at embryonic day (E) 14 (named as embWPC), in both wild type and TCA-GFP mice[14], in which thalamocortical projections are labeled with green fluorescent protein (GFP). At this stage, trigeminal nerve axons have just begun to target the principal trigeminal sensory nucleus (PrV) in the brainstem (**Figure S1A**), but PrV neuron axons have not yet entered the ventral posteromedial (VPM) thalamic nucleus[15-19].

Analysis of the snout at E18 confirmed the specific ablation of the mystacial whiskers and follicles (**Figure 1A**), with a strong reduction of whisker pad-innervating primary trigeminal sensory axons targeting the PrV (**Figure S1B**). At early postnatal stages, the total areas of PrV, thalamic ventral posterior nucleus (VPN) and S1, including other somatosensory body representations apart from the snout, did not exhibit

101 significant differences in embWPC, as compared to control mice (**Figures S2A-S2C**). In
102 contrast, the size of the areas corresponding to mystacial and upper lip whiskers
103 significantly rescaled in embWPC mice at all levels of the pathway, suggesting intra-
104 modal plasticity of connectivity. For example, in S1, we found a 54% decrease in the
105 PMBSF territory, and a 34% expansion of the ALBSF territory, a phenomenon already
106 observed at P4 (**Figures 1B** and **S2D**). Notably, we found no discernible differences in
107 the total upper lip volume, nor in the volume and number of upper lip follicles between
108 control and embWPC mice both at E18 and P8 (**Figure 1A**; **Videos S1** and **S2**). Dye
109 depositions in the cortical PMBSF or ALBSF of P8 embWPC confirmed a similar intra-
110 modal remapping of the corresponding whisker pad input-receiving VPM (wpVPM) or
111 upper lip input-receiving VPM (ulVPM) areas in the thalamic VPM[20] (**Figure 1C**).
112 Moreover, retrogradely labeled thalamocortical neurons within each VPM sub-territory
113 maintained their expected point-to-point distribution, matching cortical topography
114 (**Figure S3**).

115 Importantly, the changes of the cortical barrel field sub-territories depended on
116 mechanisms only present before birth, since cauterization of the whisker pad at postnatal
117 day 0 (P0), referred to as P0WPC, revealed no significant territorial differences in the
118 PMBSF and ALBSF between control and P0WPC across the somatosensory stations
119 (**Figures 1D** and **S4**). As expected, there were no re-arrangements of the
120 thalamocortical axons in the P0WPC (**Figures 1E** and **S5**). Thus, there is a critical
121 window in which the cortical ALBSF area can be significantly adjusted without altering
122 upper lip receptors, suggesting that after this timepoint plasticity might arise from a
123 different strategy to compensate for sensory loss.

124

125 **Functional rescaling of ALBSF in embWPC mice occurs before birth**

126 Whisker pad stimulation *in vivo* at E18 can elicit activity in the developing PMBSF[21,22],
127 indicating that the periphery-to-cortex somatosensory pathway is already functional
128 before birth. We asked whether the anatomical changes observed in embWPC at P8

129 were detectable at prenatal stages by assessing functional reorganizations. We carried
130 out peripheral whisker pad and upper lip stimulations at E18 while recording cortical
131 calcium activity in *Emx1*^{GCaMP6f} transgenic mice, expressing GCaMP6f in cortical
132 glutamatergic neurons[22] and carrying unilateral whisker pad cauterization (**Figure 2A**).
133 Stimulations of either the whisker pad or the upper lip in the control side elicited
134 responses from clusters of cortical neurons corresponding to the putative territories of
135 the PMBSF or ALBSF, respectively (**Figure 2B**; **Video S3**). In contrast, whisker pad
136 stimulations in the cauterized side (embWPC) triggered very reduced responses in the
137 caudal-most part of the expected contralateral PMBSF ("PMBSF"), confirming the
138 anatomical reduction of this territory. Remarkably, stimulations of the upper lip in the
139 embWPC side elicited misplaced responses in the expected ALBSF ("ALBSF") that
140 notably expanded into the "PMBSF" (**Figure 2B**; **Video S4**), as compared to the control
141 side. This ectopic "PMBSF" activation was maintained at P4 when the size of responses
142 to upper lip stimulation were already refined in the control side (**Figures 2C-2E**; **Videos**
143 **S5** and **S6**). Thus, the anatomical rescaling of barrel field sub-territories seen in the
144 postnatal embWPC can be functionally detected prior to birth.
145
146 **Silencing prenatal thalamic synchronous activity does not prevent the area**
147 **rescaling of barrel field sub-territories**
148 Thalamic neurons display waves of prenatal spontaneous activity that are crucial for the
149 development of cortical barrel field maps[10,21]. Therefore, we investigated whether the
150 rescaling of barrel field territories in embWPC embryos could be due explained by
151 changes in spontaneous activity of VPM neurons. Inputs from the whisker pad at E16
152 are carried by afferents from ventral portion of the PrV (vPrV), whereas inputs from the
153 upper lip are carried by afferents from dorsal PrV (dPrV)[17-19]. While at this prenatal stage,
154 vPrV afferents topographically target the dorsolateral VPM (the prospective wpVPM),
155 dPrV afferents target not only the ventromedial part (the prospective ulVPM) but cover
156 most part of the VPM[17,19]. Thus, while whisker pad and upper lip inputs are segregated

157 at the brainstem nuclei, dPrV and vPrV axons terminals prenatally overlap within the
158 prospective wpVPM territory[17,19] (**Figures 3A** and **S6**). Remarkably, despite this axonal
159 overlap, spontaneous activity patterns at E16 were sub-territory specific. We detected a
160 notable distinction in the frequency of spontaneous activity waves between the
161 prospective wpVPM and ulVPM regions. While wpVPM exhibited a high frequency of
162 waves, the prospective ulVPM showed significantly reduced frequency (**Figures 3B** and
163 **3C**; **Video S7**). In embWPC, we observed a significant change in this spontaneous
164 activity pattern, with a striking increase in thalamic waves frequency within the
165 prospective ulVPM, resembling the pattern observed in the control wpVPM primordium
166 (**Figure 3B** and **3C**; **Video S8**). Thus, during prenatal development whisker input
167 deprivation remaps spontaneous neuronal activity patterns in the future ulVPM territory.
168 Next, we asked whether the embryonic increased activity in the prospective
169 ulVPM might influence the functional and anatomical rescaling of the ALBSF territory.
170 Thus, we tested this possibility and conducted embryonic whisker pad cauterization in a
171 mouse in which the synchronous spontaneous activity of the thalamus is embryonically
172 disrupted (referred to as embWPC-Th^{Kir})[21]. Briefly, we used a tamoxifen-dependent
173 $Gbx2^{CreERT2}$ mouse with a floxed line expressing the inward rectifier potassium channel
174 2.1 (*Kcnj2*) fused to the mCherry reporter in thalamic neurons (referred to as Th^{Kir}). Our
175 data revealed that thalamic and cortical territories in embWPC-Th^{Kir} mice exhibited a
176 spatial reorganization similar to that observed in embWPC mice. In both mice, the
177 wpVPM and PMBSF territories virtually disappeared, and the ulVPM and ALBSF
178 expanded as compared to the control (**Figure 3D**). Consistent to previous studies in the
179 Th^{Kir} mouse[21], manipulating thalamic activity patterns in the embWPC mice (embWPC-
180 Th^{Kir}) resulted in the absence of thalamic waves (**Figures S7A** and **S7B**) and, the
181 complete loss of barrels, evidenced by a total lack of TCA clustering, in both PMBSF and
182 ALBSF territories (**Figures 3D** and **3E**). The rescaling of thalamocortical circuits was
183 also detected in the embWPC-Th^{Kir} mouse, but not in the Th^{Kir} mouse alone, as
184 evidenced by dye tracing studies (**Figures 3E** and **S7C**). In sum, our results demonstrate

185 the patterns of spontaneous activity in prenatal VPM neurons are dispensable for intra-
186 modal thalamic and cortical sub-territories rescaling to input deprivation.
187
188 **Upper lip input-receiving thalamic neurons adopt a similar transcriptional profile**
189 **to mystacial input-receiving neurons**
190 Cross-modal and intra-modal changes in the transcriptional programs of thalamic
191 neurons have been shown to generate thalamocortical circuit re-organizations and
192 cortical adaptations, as shown in early blind pups or in mice with an embryonic ablation
193 of the VPM nucleus[10,23,24]. Therefore, we examined whether the anatomical and
194 functional circuit expansion of the ALBSF in embWPC might be influenced by changes
195 in the transcriptional program of VPM neurons. To assess this, we dissected tissue, at
196 similar distances from the dorsal lateral geniculate (dLG) nucleus, from wpVPM and
197 ulVPM in control and embWPC mice at P0 (**Figure 4A**) and compared their
198 transcriptional profiles by bulk RNA-sequencing (RNA-seq). Principal component
199 analysis (PCA) revealed that the transcriptomes from wpVPM and ulVPM cells in control
200 mice clustered separately already at P0 (**Figure S8A**). Differential Expression Analysis
201 (DEA) further revealed 377 Differentially Expressed Genes (DEGs) enriched in the
202 wpVPM as opposed to 365 in the ulVPM cells. Among the DEGs enriched in each
203 population, we found genes previously identified as being involved in somatosensory
204 development such as *Epha3, Sox2, Hs6st2, Cdh8 or Ror*α enriched in wpVPM[24-28] or
205 *Ror*β*, Slitrk6, Foxp2, Calb1 or Lhx2*[10,29-32] enriched in the ulVPM (**Figures S8B** and **S8C**;
206 **Table S1**).
207 Then, we compared control versus embWPC transcriptional programs in the
208 VPM. Remarkably, PCA analysis from ulVPM cells in embWPC mouse indicated that
209 these neurons grouped more closely with control wpVPM than control ulVPM (**Figures**
210 **4B** and **S8D**). This transcriptional shift was appreciated when the expression pattern of
211 the upper lip and whisker-pad DEGs was plotted in the ulVPM of the embWPC (**Figure**
212 **4C**). To investigate this effect, we trained a Support Vector Machine (C-SVM) classifier

213 using region-specific genes and compared the results with the ulVPM-embWPC. This
214 machine learning approach predicted that the cauterized model would be classified as
215 the wpVPM control in 70% of cases, compared to 30% for the ulVPM control (**Figure**
216 **4D**). Additionally, DEA against the wpVPM control revealed a much lower number of
217 differentially expressed genes (93 DEGs) compared to the ulVPM control (268 DEGs)
218 (**Figure 4E**).

219 In total, 150 region-specific DEGs from ulVPM and wpVPM where significantly
220 changed by the embWPC (**Figure 4F**). Namely, in the ulVPM of the embWPC mouse,
221 we observed an upregulation of approximately 17% of the DEGs normally expressed in
222 the control wpVPM and a downregulation of about 23% of control ulVPM DEGs,
223 respectively (**Figures 4F** and **S8E**; **Table S2**). Notably, genes such as *Rorα, Epha4,*
224 *Hs6st2, Cdh9,* or *Plxna2*, involved in axon guidance, thalamocortical mapping and
225 wpVPM development[26,33], exhibited a wpVPM-like pattern in the ulVPM of embWPC mice
226 (**Figures 4G** and **S8F**), also corroborated by *in situ* hybridization (**Figures 4H** and **S8G**).
227 Next, we performed a Gene Ontology (GO) functional enrichment analysis of the genes
228 with expression changes in the ulVPM of the embWPC and identified 11 clusters of GO-
229 Terms enriched in Biological Processes (BP) and Molecular Functions (MF) (**Figure S9**;
230 **Table S3**). The top ranked cluster included 99 genes (46,8%) enriched in BP involved in
231 dendrite development or synapse assembly (e.g. *Robo1, Flrt3*), and 12 genes (18,8%)
232 enriched in MF involved in voltage-gated channel activity (e.g. *Kcnc2, Kcnab1*). In
233 summary, the spatial rescaling of cortical ALBSF territory in embWPC correlates with
234 transcriptomic changes observed in upper lip thalamic input neurons, which shift towards
235 a molecular signature resembling that of whisker pad input neurons (**Figure 4I**).
236

237 **Increase of barrel size and functional spatial resolution of the cortical ALBSF map**
238 We investigated whether upper lip-recipient thalamic neurons that acquire a whisker pad
239 transcriptional profile during perinatal development might develop additional PMBSF
240 characteristics later in life. At P8, PMBSF and ALBSF cortical areas differ in the average

241 size of their barrels and the extent of clustering of thalamocortical axons. Remarkably,
242 we observed that, in addition to the overall increase in the cortical area occupied by the
243 ALBSF, the average size of the cortical individual barrels in the ALBSF of the embWPC
244 was significantly larger compared to the ALBSF control (**Figure 5A**). This change
245 appears to follow a gradient, with the largest ALBSF barrels located nearest to the
246 remaining PMBSF. Furthermore, the cortical map of the expanded ALBSF gained
247 definition and contrast as thalamocortical terminals appeared more clustered within each
248 barrel, and less innervating the barrel septa, resembling the control PMBSF (**Figures**
249 **5B-5D**). These differences in barrel size and contrast in the ALBSF map of the embWPC
250 where not detected in P0WPC mice (**Figures 5A** and **5B**).

251 Since thalamocortical input is a primary regulator of region-specific cortical
252 features, we investigated whether other cortical characteristics, besides barrel size and
253 thalamocortical clustering, had also changed in the ALBSF cortex of the embWPC. The
254 postnatal PMBSF is known to contain fewer parvalbumin (PV) expressing interneurons
255 in layer IV compared to the ALBSF[34]. Like in the PMBSF, we found significantly fewer
256 PV-positive interneurons both in barrels and septa in layer IV of the ALBSF in the
257 embWPC as compared to the ALBSF control (**Figure 5E**). Hence, our findings
258 demonstrate that, irrespective of receiving input from upper lip peripheral receptors, the
259 VPM territory in embWPC adopts a molecular identity akin to that of a territory receiving
260 input from mystacial whiskers. Consequently, it gains specific features of that circuit,
261 including increased barrel size, better anatomical map definition, and fewer layer IV PV
262 interneurons (**Figure 5F**).

263 Next, we tested whether these anatomical reorganizations might have a
264 functional correlate, as for example an enhanced topographical spatial resolution to
265 upper lip stimulation. Thus, we carried out multi-point stimulations within the whisker pad
266 or upper lip on both control and embWPC mice at P4 (**Figure 6A**). On the control mice,
267 cortical evoked responses confirmed a topographic organization of both PMBSF and
268 ALBSF responses; however, while the PMBSF responses exhibited a well-defined and

269 precise organization with virtually non-overlapping responses, those of the ALBSF were
270 broader and less refined in comparison (**Figure 6B**; **Video S9**). Thus, beyond their
271 anatomical idiosyncrasies, cortical barrel sub-fields also have a distinct degree of
272 functional map definition as they emerge during perinatal development. Interestingly,
273 stimulations from distinct locations of the upper lip of embWPC mice resulted in
274 significantly less overlapping responses within the ALBSF (**Figure 6B**; **Video S10**),
275 suggesting an enhanced spatial discrimination in the ALBSF of embWPC akin to that
276 seen in the control PMBSF map.

277 Finally, we investigated whether the rescaled ALBSF with enhanced resolution of
278 in the embWPC mice takes on PMBSF functions during somatosensory behavior in
279 adulthood. To do this, we conducted cFOS staining to label stimulated neurons in the
280 ipsilateral and contralateral barrel sub-fields of embWPC mice after 10 minutes of
281 exploring an enriched environment at P60 (**Figure 6C**). Our immunostaining for cFOS
282 revealed that, whereas in the ipsilateral (control) side the ALBSF was barely activated
283 as compared to the PMBSF, the ALBSF was the predominantly activated region in the
284 contralateral (cauterized) side after exploration. These results strongly suggest that the
285 remapped ALBSF neurons of the embWPC mouse play a prominent role in vibrissae-
286 driven sensory behavior in the adult.

287

288

289 **DISCUSSION**

290 Our study underscores the existence of a prenatal temporal window during mouse brain
291 development that allows for the tuning of the size and definition of somatosensory cortical
292 representations. Before cortical barrel fields are anatomically apparent, the thalamic
293 VPM sub-territories exhibit specific transcriptional signatures at birth. Our results suggest
294 that these signatures contribute to the distinct intra-modal anatomical and functional
295 circuitry features specific to PMBSF and ALBSF cortical sub-territories.

296 Furthermore, our findings suggest that modulations in these transcription
297 programs might enable intra-modal plasticity changes independently of the type of
298 peripheral receptors. In mice lacking the mystacial whiskers, VPM neurons receiving
299 upper lip whisker input can shift their transcriptional features toward a whisker pad-like
300 program, reconfiguring thalamocortical circuits and cortical features to resemble a
301 PMBSF. These changes increase barrel size and functional spatial resolution, thereby
302 enhancing spatial discrimination in regions such as the ALBSF, where cortical
303 representations were otherwise less defined.

304 The developmental relationship between sensory receptors and somatosensory
305 representations has been thoroughly examined in prior work involving mice and rats.
306 Embryonic ablation of the forelimb in rats resulted in the expansion of S1 representation
307 of the hindlimb without altering the sensory receptors of the spared peripheral region[35].
308 Moreover, deprivation of a single whisker or a row of whiskers during the first postnatal
309 week, leads to the loss of the corresponding cortical barrels and enlargement of the
310 surrounding barrels[36-41]. And remarkably, rewiring of ipsilateral trigeminal input from
311 mystacial whiskers to the ipsilateral barrel field generates an ectopic barrel field within
312 the normal barrel map[42]. Collectively, these studies highlight the sensitivity of
313 somatosensory regions and barrel maps to manipulations in peripheral or sensory input
314 but also questioned a direct correlation between the size of cortical barrels and their
315 corresponding peripheral sensory receptors. Our results in the embWPC model define a
316 developmental window for an intra-modal barrel field reorganization, showing that only
317 embryonic, and not postnatal, ablation of the whisker pad induces the ALBSF anatomical
318 and functional enlargement. This reorganization capability is therefore temporally
319 constrained during prenatal development and anticipates the closure of the critical time
320 window for somatosensory circuits[38,43].

321 Thalamic spontaneous activity is key for the emergence of cortical
322 somatosensory maps, as evidenced by the fact that suppressing this activity leads to
323 mice that do not develop barrels despite having normal whiskers[21]. Moreover, in early

324 blind pups, changes in activity-dependent gene regulation in VPM neurons correlate to
325 changes in barrel size[10]. Using embWPC, we could show that the enlargement of the
326 cortical ALBSF area is guided by the thalamus in an activity-independent manner.
327 Indeed, in embWPC-*Th*^{Kir} mice, which lack synchronous thalamic activity, the rescaling
328 of the ALBSF still occurs. On the other hand, similarly to what occurs cross-modally in
329 early blind pups between the dLG and the VPM[10], we observed a striking intramodal
330 reorganization of the frequency and pattern of thalamic waves between VPM sub-fields
331 in embWPC mice. The ulVPM significantly increased the frequency of thalamic waves
332 compared to control mice. This change in activity pattern might serve as a mechanism
333 to enhance ulVPM barrel size and definition and, in turn, to map these activity-dependent
334 features onto the cortical ALBSF during development. This hypothesis could not be
335 directly tested, as thalamocortical axons in the embWPC-*Th*^{Kir} mice fail to cluster in layer
336 IV in both PMBSF and ALBSF, as previously described in *Th*^{Kir} mice[21].

337 Remarkably, our study revealed that thalamic neurons can shift their
338 transcriptional profile intra-modally. We found that the transcriptional profile of ulVPM
339 neurons in embWPC mice mirrors that of the wpVPM neurons in control mice. Crucial
340 genes for thalamocortical barrel field development, such as *Ror*α or *Epha4*[26,33],
341 accordingly altered their expression pattern in the ulVPM neurons innervating the
342 ALBSF. For instance, we observed an upregulation of *Ror*α in this region, suggesting a
343 potential role in increasing the density and clustering of axonal terminals in layer IV in
344 the ALBSF of the embWPC mice. An activity-dependent upregulation of *Ror*β, a related
345 orphan receptor, in VPM neurons has been shown to mediate an increased clustering of
346 thalamic axons in S1[10]. ulVPM neurons adopting a region-specific wpVPM transcriptional
347 profile might serve as an intrinsic mechanism to switch a PMBSF developmental
348 program, ensuring an enhanced anatomical and functional definition of thalamocortical
349 axons in the ALBSF cortical barrel map. Additionally, we identified alterations in genes
350 directly associated with neuronal activity[44,45], including ion channels, which may

351 contribute to or reflect the modified pattern of thalamic activity observed in the embWPC
352 model. Yet, it remains to be determined whether the acquisition of wpVPM-like molecular
353 identity by ulVPM neurons is dependent on thalamic spontaneous activity.

354 Large barrels in the PMBSF correspond to long mystacial whiskers[12,13], whereas
355 ALBSF barrels relate to the short whiskers on the upper lip of the snout and are
356 comparatively smaller, less defined and densely packed[9,46,47]. Moreover, although the
357 average volume of a single barrel in the ALBSF is smaller than in the PMBSF, the
358 numerical density of parvalbumin (PV)-positive interneurons is higher in ALBSF than in
359 the PMBSF[34]. Somata of PV neurons in the barrels and septa of the ALBSF are reported
360 to receive more vesicular glutamate transporter Type 2–labeled (vGlut2) boutons than
361 those in the PMBSF, suggesting the presence of more potent feedforward inhibitory
362 circuits in the ALBSF[34]. Behaviorally, mystacial vibrissae hold significant behavioral
363 relevance for the animal, being the first ones used for search of objects and gaps, and
364 to discern diverse tactile features such as object position, shape, or texture[48]. Although
365 the function of upper lip shorter whiskers remains largely unexplored, they appear to
366 primarily aid in object discrimination when the snout is near the object[8,49-51]. Given these
367 anatomical and functional disparities, the PMBSF and ALBSF represent two distinct
368 somatosensory subsystems. Consequently, we initially expected minimal reorganization
369 of the ALBSF upon deprivation of the whiskers corresponding to the PMBSF. However,
370 our data from the embWPC mice revealed a notable anatomical reorganization within
371 the ALBSF, leading to the formation of large and well-defined barrels and an increased
372 density of PV interneurons at the postnatal life. Additionally, our *in vivo* functional data
373 revealed that this reorganization might contribute to enhance functional resolution of the
374 ALBSF map to point-to-point peripheral stimulations.

375 Altogether, these findings highlight a decoupling of mechanisms governing the
376 type, size, and density of sensory peripheral receptors from those influencing the size
377 and definition of cortical representations that might involve adopting subcortical- and
378 subregion-specific transcriptional programs. Specifically, we observed that the prenatal

brain possesses plasticity mechanisms to develop a barrel field with anatomical and functional features akin to the PMBSF, regardless of the type of peripheral receptor. Therefore, our findings indicate that the brain may still construct a barrel map capable of processing intricate tactile functions for the animal, even in scenarios involving the availability of only small receptors with subsidiary functions.

384 **Methods**

385 **Mouse strains**

386 All animal experiments were conducted in accordance with the Committee on Animal
387 Research at the University Miguel Hernández that approved all the animal procedures,
388 which were carried out in compliance with Spanish and European Union regulations.
389 Similar numbers of male and female mice were used interchangeably. No sex-related
390 differences were observed in the measurements throughout the study. Mice were
391 maintained in pathogen-free facilities under standard housing conditions with continuous
392 access to food and water on a 12h light-dark cycle. The number of animals used in each
393 experiment is noted in the figure legends.

394 All mouse transgenic lines in this study were maintained on an ICR/CD-1 genetic
395 background and genotyped by PCR. The *TCA-GFP Tg*, in which the TCAs are labelled
396 with GFP, the $R26^{Kir2.1\text{-}mCherry}$, mouse lines were previously described[10,14,21]. The Cre-
397 dependent mouse line, $R26^{GCaMP6f}$ was obtained from Jackson Laboratories (Stock
398 number 024105) and crossed with an $Emx1^{Cre/+}$ transgenic mouse[52] to conditionally
399 express the fast calcium indicator GCaMP6f in glutamatergic cortical neurons
400 ($Emx1^{GCaMP6f}$)[21,22]. The $R26^{Kir2.1\text{-}mCherry}$ mice were crossed with an inducible Cre^{ERT2}
401 mouse line driven by *Gbx2*, an early specific thalamic promoter ($Gbx2^{CreERT2/+}$)[53]. Double
402 mutants are referred as Th^{Kir} and triple mutants as $TCA\text{-}GFP\text{-}Th^{Kir}$ [21]. Tamoxifen
403 induction of Cre recombinase in the double/triple mutant embryos was performed by
404 gavage administration of tamoxifen (5 mg dissolved in corn oil, Sigma) at E10 to
405 specifically target all primary sensory thalamic nuclei. Tamoxifen administration in
406 pregnant mice produces non-desirable side effects such as delivery problems and
407 decrease survival of newborn pups[54]. To increase the survival rate of young pups, we
408 administered 125 mg/Kg of progesterone (DEPO-PROGEVERA®) intraperitoneally at
409 E14 and implemented C-section procedure at E19. Pups were then placed with a foster
410 mother. In all cases, the Cre^{ERT2}-negative littermates were used as controls of the
411 experimental condition. The $r2^{mCherry}$ [19], $Krox20^{Cre}$ [55] and *R26RZsGreen* (Jackson

412 Laboratories, Stock number 007906)[56] lines, were as described. We crossed *Krox20*^{Cre}
413 with *R26RZsGreen* to generate double transgenic *Krox20*^{ZsGreen} mice and we also
414 generated *Krox20*^{ZsGreen}*::r2*^{mCherry} triple transgenic mice.
415
416 **Histology**
417 For *in situ* hybridization and immunohistochemistry at postnatal stages, mice were
418 perfused with 4% paraformaldehyde (PFA) in PBS (0.01 M), and their brains were
419 subsequently removed and post-fixed in the same fixative overnight. For
420 immunohistochemistry of embryonic tissue, the brains were dissected out and
421 immediately fixed in 4% PFA overnight. For Nissl staining, a microtome (MICROM) was
422 used to cut paraffin slices of 5 μm. Next, the sections were stained in 0.5% cresyl violet
423 (Sigma) solution for 15-25 min and then rinsed quickly in distilled water. After
424 decolorization in 70% ethyl alcohol for few seconds, the sections were dehydrated in
425 95%, 100% ethyl alcohol for 2 to 3 min, cleared in xylen (Sigma) for 2 min and mounted
426 with Eukitt (Merk). Cytochrome oxidase staining was performed to label the PrV
427 territories. For cytochrome Oxidase (CytOx) staining, 80 μm vibratome coronal sections
428 were incubated overnight at 37 ºC in a CytOx solution: 0.03% cytochrome c (Sigma
429 C2506), 0.05% 3-3′ diaminobenzidine tetrahydrochloride hydrate (DAB, Sigma D5637)
430 and 4% sucrose in PBS. For tangential sections, cortical hemispheres were flattened
431 and cryoprotected through steps of 10%, 20% and 30% of sucrose in PBS. Then, a
432 cryotome (MICROM) was used to cut at 80 μm tangential sections.
433 Immunohistochemistry was performed on 80 μm vibratome or cryotome brain sections
434 (coronal and tangential), which were first incubated for 1h at room temperature in a
435 blocking solution containing 1% BSA (Sigma) and 0.25% Triton X-100 (Sigma) in PBS.
436 Afterwards, the slices were incubated overnight at 4 °C with the following primary
437 antibodies: guinea pig anti-vGlut2 (1:10000, Synaptic Systems, 135404), chicken anti-
438 GFP (1:3000; Aves Labs, GFP-1020), rat anti-RFP (1:1000, Chromotek, 5F8), rabbit

439 anti-cFos (1:500, Synaptic Systems, 226003), rabbit anti-PV (1:5000, Swant PV27), and
440 rabbit anti-RFP (1:1000, Rockland, 600-401-379). Sections were then rinsed in PBS and
441 incubated for 2h at room temperature with secondary antibodies: Alexa488 donkey anti-
442 guinea pig (1:500, ThermoFisher, A11073), Alexa488 goat anti-chicken (1:500,
443 ThermoFisher, A11039), Alexa594 donkey anti-rat (1:500, ThermoFisher, A21209) and
444 Alexa goat 568 anti-rabbit (1:500, Invitrogen, A11011). Counterstaining was performed
445 using the fluorescent nuclear dye 4′,6-diamidino-2-phenylindole (DAPI) (Sigma). In situ
446 hybridization was performed on 60 μm vibratome sections using digoxigenin-labelled
447 antisense probe for *Rorα*, *Epha4*, *Pou2f2*, *Hs6st2*, *Plxna2* and *Cdh9*. Hybridization was
448 carried out overnight at 65 ºC, and after hybridization, the sections were washed and
449 incubated overnight at 4 ºC with an alkaline phosphatase-conjugated anti-digoxigenin
450 antibody (1:2500-1:4000, Roche). To visualize the RNA-probe binding, colorimetric
451 reaction was performed for 1-2 days at room temperature in a solution containing NBT
452 (nitro-blue tetrazolium chloride, Roche) and BCIP (5-bromo-4-chloro-30-indoly
453 phosphate p-toluidine salt, Roche). After development, the sections were washed and
454 mounted in Glycerol Jelly (Merck Millipore). Images were acquired with a Leica DFC550
455 camera into a Leica DM5000B microscope, Leica K5 camera into Leica DMi8
456 microscope or with an Axioscan Z1 widefield microscope (Zeiss).
457

458 **Immunolabeling-enabled three-dimensional imaging of solvent-cleared organ**
459 **(iDISCO+)**

460 Whole mount for the iDISCO+ protocol was conducted following the previously described
461 methods[57,58]. After perfusing mice with 4% PFA, heads (without any dissection) were
462 dehydrated using a series of methanol concentrations (50, 80, 100, and 100%) and
463 subsequently incubated overnight in 6% H_2O_2 in methanol to bleach the samples.
464 Following this, heads were blocked with PBS-GT (0.5% Triton X-100, 0.2% gelatin) for 4
465 days. For the clearing process, heads underwent dehydration in methanol (20, 40, 60,
466 and 80%) at room temperature on a rotating shaker. Specimens were then immersed

467 twice in 100% methanol for 1 hour and treated overnight in 1/3 volumes of 100%
468 dichloromethane (DCM; Sigma-Aldrich; 270997). The subsequent day, heads were
469 incubated in 100% DCM for 30 minutes. Finally, samples were cleared in 100% dibenzyl
470 ether (DBE; Sigma-Aldrich; 108014) until they became translucent.
471
472 **Ultramicroscopy and Image Processing**
473 3D imaging was primarily performed with an ultramicroscope I (LaVision BioTec) using
474 ImspectorPro software (LaVision BioTec). The light sheet was generated by a laser
475 (wavelength 488 nm, LaVision BioTec). A binocular stereomicroscope (MXV10,
476 Olympus) with a 23x objective (MVPLAPO, Olympus) was used at different
477 magnifications (1.25x). Samples were placed in an imaging reservoir made of 100%
478 quartz (LaVision BioTec) filled with ethyl cinnamate and illuminated from the side by the
479 laser light.
480 Images were generated using Imaris x64 software (version 9.3.1, Bitplane). Stack
481 images were first converted to Imaris files (.ims) using ImarisFileConverter. The whisker
482 pad and upper lip areas reconstruction were generated by creating a mask around each
483 one using the "surface tool" and they were pseudo-coloured (whisker pad area in
484 magenta and upper lip area in cyan). Each individual follicle was isolated also manually
485 using the same tool, selecting nine follicles arbitrarily at three different points from medial
486 to lateral. The septa volume reconstruction from coronal sections of 80 μm was
487 generated by creating masks around each barrel using the "surface tool" and they were
488 pseudo-coloured (orange).
489
490 ***In utero* and postnatal unilateral whisker pad cauterization**
491 Embryonic unilateral whisker pad cauterization (embWPC) was performed at E14 as
492 described previously for enucleation[10]. Dams were deeply anesthetized with isoflurane
493 and the uterine horns were exposed through a midline laparotomy. After cauterizing right
494 whisker pad side in half of the litter, the embryos were returned to the abdominal cavity,

495 the surgical incision was closed, and the embryos were allowed to develop until either
496 E18 or postnatal stages. Postnatal unilateral whisker pad cauterization (P0WPC) was
497 performed on P0 pups. Animals were deeply anaesthetized on ice. The right whisker pad
498 was cauterized under the loupe to specifically burn the principal whiskers follicles. Pups
499 were then warmed up to 37ºC on a heating pad, before being returned to the mother.
500

501 **Measurement of brain areas and data analysis**

502 ImageJ software was used to measure the size of individual barrels, barrel field
503 territories in the cortex, thalamus and brainstem, as well as the snout areas in slices. For
504 barrel field territories and snout areas data were normalized. Each barrel field or snout
505 area from a given experimental condition was normalized to the corresponding barrel
506 field or snout mean area in the control, which was considered as 1. For the snout
507 measurements, the skin of the snout was flattened and post-fixed in 4% PFA. Paraffin
508 slices of 5 μm were obtained to quantify the number of follicles and the upper lip snout
509 area using Nissl staining. We measure two slices per animal, one medial and one more
510 lateral, and calculated the average. TCA-GFP mouse was used for the quantifications of
511 the barrel field definition in flattened tangential sections, barrel field areas *in toto* and
512 thalamic territories in slices. To quantify the size of cortical areas *in toto*, TCA-GFP
513 (control, embWPC, P0WPC and embWPC-Th^{Kir}) mice were perfused and directly
514 processed to obtain images under the stereo fluorescent microscope (Leica MZ10 F).
515 Coronal serial slices of 80 μm were obtained from TCA-GFP brains, and thalamic barrel
516 field territories were immunolabel with GFP and vGlut2 in order to better detect the areas.
517 For $\Delta F_b/F_s$ quantifications, we used ImageJ to measure the gray value of EGFP labelling
518 in barrels of flattened tangential sections. $\Delta F_b/F_s$ was calculated using the maximum
519 value of the baseline signal average as F_s in single barrels. To measure the gray value,
520 we used a 20-width segmented line, covering 5 barrels per condition, and calculated the
521 average. To compare the barrel profile for the different conditions, we normalized each

522 barrel´s gray values to the lowest number (septa), which was considered as 0. Next, we
523 took 11 gray value data points per barrel to normalize the length for all the conditions.
524 To quantify the mean gray value in septa, coronal serial slices of 80 μm were obtained
525 from TCA-GFP brains, and barrels from PMBSF and ALBSF (control and embWPC)
526 were immunolabel with GFP to measure the fluorescence of three barrels septa per
527 condition using Imaris x64 software, and calculated the average. For PV+ cells
528 quantifications in PMBSF and ALBSF barrels and septa, we counted the number of PV+
529 cells within four barrels and their septa for each condition in flattened tangential sections
530 of 80 μm immunolabel with PV and vGlut2. We quantified cFos expression within PMBSF
531 and ALBSF layer IV. The region of interest (ROI) was a square of 600x1000 μm on each
532 territory measuring the mean gray value.
533
534 **Dye-tracing studies**
535 For axonal tracing, animals were perfused with 4% PFA in PBS. Heads were post-fixed
536 overnight to trace innervation from the snout to the trigeminal nucleus, while brains were
537 dissected and post-fixed overnight to trace thalamocortical axons. Small DiI (1,1′-
538 dioctadecyl 3,3,3′,3′-tetramethylindocarbocyanine perchlorate; Invitrogen), DiA (4-[4-
539 (dihexadecylamino) styryl]-N-methylpyridinium iodide; Invitrogen) and DiD (1,1'-
540 Dioctadecyl-3,3,3',3'-Tetramethylindodicarbocyanine, 4-Chlorobenzenesulfonate Salt;
541 Invitrogen) crystals were inserted under a stereo fluorescence microscope (MZ10 F,
542 Leica) into the PMBSF, ALBSF, the whisker pad and upper lip. The dye was allowed to
543 diffuse at 37 °C in PFA solution for 4 to 8 weeks to trace the innervation from the snout
544 to the PrV. To trace the thalamocortical pathway, small DiI and DiA crystals were inserted
545 into distinct PMBSF barrels (C2, C3, D3 and C4) and DiI, DiA and DiD crystals were
546 placed into ALBSF territory. To reveal the PBMSF and ALBSF, a TCA-GFP transgenic
547 specific mouse line was used. The dye was allowed to diffuse at 37 °C in PFA solution
548 for 3 weeks. Vibratome sections (80 μm thick) were obtained and counterstained with

549 the fluorescent nuclear dye DAPI (Sigma-Aldrich). Three sections per animal were
550 imaged using a Leica K5 camera into Leica DMi8 microscope. Image analysis was
551 performed on ImageJ. To quantify the translocation of the backlabeling in the VPM, the
552 distance from the dorsolateral geniculate (dLG) nucleus border was measured to the
553 center of the backlabeled cells in the VPM. The distance from the dLG nucleus border
554 to the separation between wpVPM and ulVPM was determined following the barreloids
555 rows in the VPM of ctrl mice.
556
557
558 **Measurement of PrV axons overlap in VPM and data analysis**
559 To label rhombomere 3-derived vPrV neurons, we used the *Krox20*^{Cre} line[55] to drive the
560 Rosa-Zsgreen reporter (*R26RZsGreen*)[59], whereas to label rhombomere 2-derived dPrV
561 neurons, we used the *r2*^{mCherry} reporter line[19]. Brains from *Krox20*^{Cre}; *R26RZsGreen*;
562 *r2*^{mCherry} animals, in which vPrV and dPrV projections are labeled simultaneously, were
563 collected at embryonic stages (E16.5, E18.5) and postnatal stages (P0, P4, P8) for
564 analysis. Embryonic brains were directly post-fixed in 4% PFA in PBS, while postnatal
565 brains were perfused before post-fixation in the same fixative. Brains were cut on a
566 Vibratome (Leica) at 60 μm thickness throughout the VPM and PrV. To enhance the
567 r2::mCherry signal, the sections were stained with a rabbit anti-RFP primary antibody
568 (1:1000, Rockland, 600-401-379) coupled to an anti-rabbit Alexa 568 secondary
569 antibody (1:500, Invitrogen, A11011), while the endogenous Zsgreen fluorescence was
570 not amplified. At least five sections per animal were imaged using Axioscan Z1 widefield
571 microscope (Zeiss), using a 10x (NA=0.45) plan-APOCHROMAT objective. Subsequent
572 image analysis was conducted using ImageJ. To quantify the percentage of overlap of
573 vPrV-dPrV axons in the VPM, wand tool connecting pixels of the same intensity level in
574 a 15-pixel range, was used to automatically delineate the innervation area of Krox20+
575 and R2+ axons, generating the Regions of Interest (ROIs). Subsequently, the
576 overlapping area and the total innervation area of both Krox20+ and R2+ axons were

577 measured with the measure tool in ImageJ to calculate the percentage of overlap of PrV
578 axons in the VPM. The same strategy was used for PrV dye tracings to measure the
579 overlap between dPrV and vPrV axons in the VPM.
580
581 ***In vivo* mesoscale calcium imaging**
582 As previously described[22], embryos at E18 were extracted from the uterus and
583 maintained at 35 ºC. E18 pups were immobilized using soft clay. P4 mice underwent
584 anesthesia with ice, followed by surgical removal of the scalp. A 3D-printed plastic holder
585 was attached to the skull using cyanoacrylate adhesive and dental cement, then affixed
586 to a ball-joint holder to stabilize the head. To maintain body temperature, pups were
587 placed on a controlled temperature heating pad, ensuring a range of 32-34 ºC. For
588 recording calcium activity, we used a 16-bit CMOS camera (ORCA-Flash 4.0,
589 Hamamatsu) coupled to a stereo microscope (Stereo Discovery V8, Zeiss), which
590 offered 470 nm LED illumination. For *Emx1*^{GCaMP6f}, images were acquired with a frame
591 size of 1024x1024 pixels using a macro magnification of 1.6x at E18 and of 1.25x at P4,
592 resulting in spatial resolution of 8.12 µm/pixel and 10.64 µm/pixel, respectively. Image
593 frames were captured continuously at a rate of 3.33 frames per second (300 ms frame
594 period) for *Emx1*^{GCaMP6f} with an average of 3 movies was acquired per animal.
595
596 ***In vivo* mechanical stimulation of the whisker pad**
597 We conducted somatosensory stimulations by touching the whisker pad and upper lip
598 using a 0.16 g von Frey filament (TouchTest®, BIOSEB). Each animal was stimulated at
599 least three times, with intervals of 5 minutes between each stimulus. Subsequently, we
600 calculated the size of responses in the PMBSF and ALBSF elicited by whisker pad and
601 upper lip stimulations.
602
603 **Analysis of the evoked activity *in vivo***

604 For the assignment of cortical territories, the perimeters of the PMBSF and ALBSF were
605 determined using the cortical responses elicited by mechanical stimulation of five sites
606 on the whisker pad, as previously described[21,22] and two sites of the upper lip. At
607 embryonic day (E)18, the perimeters were predicted by scaling down and superimposing
608 the limits of the sensory territories observed in the TCA-GFP transgenic line[14] at P2, as
609 previously detailed[22], and using the responses to whisker pad and upper lip stimulations
610 as reference for PMBSF and ALBSF, respectively. Image analysis was performed with
611 ImageJ. The mean fluorescence of five frames just prior to the stimulation established
612 F0 (baseline fluorescence), and a $\Delta F/F0$ time series was then generated from the raw
613 data and subsequently transformed into 8-bit images before processing with a 2-pixel
614 diameter Gaussian filter. A maximum intensity projection of all frames containing evoked
615 responses was obtained. The boundaries of the response were defined using the wand
616 tool, connecting pixels of the same intensity level within a 15-pixel range, and the area
617 of each response was calculated using the measure tool in ImageJ. To measure the
618 active fraction of PMBSF and ALBSF in embWPC mice at E18 and P4, the control side
619 was used to delineate the PMBSF and ALBSF territories following stimulation of the
620 whisker pad or upper lip, respectively. On the WPC side, these areas were superimposed
621 using the mirror image from the control side. The PMBSF and ALBSF active fractions
622 were determined by measuring all elicited responses within each territory and calculating
623 the percentage of the PMBSF and ALBSF theoretical areas occupied by these
624 responses following whisker pad or upper lip stimulations. To quantify the percentage of
625 overlap between responses following whisker pad and upper lip stimulations (%PMBSF-
626 ALBSF overlap) at E18 and P4, the overlap between all elicited responses following
627 whisker pad and those following upper lip stimulations was calculated. To quantify the
628 percentage of overlap within PMBSF or ALBSF (% Responses overlap) in ctrl and
629 embWPC, the overlap for two different stimuli on the whisker pad or two different stimuli
630 on the upper lip was calculated.

631 To visualize the evoked stimuli in different color profiles for the generation of
632 supplementary movies, we utilized custom scripts developed in Matlab™. These scripts
633 were adapted from the image analysis suite WholeBrainDX (referenced in the Data and
634 code availability section). For each movie, frames containing movement artifacts,
635 spontaneous activity, and calcium activity deemed as stimulation byproducts were
636 excluded. Baseline correction was performed using the built-in Matlab function
637 'msbackadj' with a window size of 20 and a step size of 20. Subsequently, $\Delta F/F0$ was
638 computed using the median value of the corrected signal as F0. Movie segmentation and
639 calcium event detection followed the method described[60]. Image segmentation and
640 generation of a binary movie involved Gaussian smoothing with an 80 μm distance and
641 a signal intensity threshold. The binary movie was color-labeled using ImageJ software
642 and customized with a Gaussian filter. Subsequently, the original movie and the color-
643 coded binary movie were merged using the 'Image Calculator' function in ImageJ.
644
645 **Microdissection and RNA isolation for RNA-seq**
646 To collect tissue from the wpVPM and ulVPM territories, ctrl and embWPC P0 pups were
647 euthanized via decapitation, and their brains were dissected out under RNase-free
648 conditions to prevent RNA degradation. The brains (five brains were pooled for each
649 sample) were collected in ice-cold KREBS solution and sliced into 300 μm sections using
650 a vibratome (VT1000S Leica). The wpVPM and ulVPM territories were rapidly
651 microdissected under a stereo microscope. The bulk tissue was immediately transferred
652 to lysis buffer of the Rneasy® Micro Kit (Qiagen, 74004) for total RNA extraction,
653 following the manufacturer's instructions. RNA quality was measured for all samples
654 using an Agilent Bioanalyzer 2100 system, and only samples with RNA Integrity Number
655 (RIN) > 8 were used for library construction.
656
657 **Library preparation and RNA sequencing**

658 Library construction and sequencing were performed at Novogene Co. Ltd. Genomics
659 core facility (Cambridge, UK). cDNA multiplex libraries were prepared using a custom
660 Novogene NGS RNA Library Prep Set (PT042) kit. Briefly, mRNA was purified from total
661 RNA using poly-T oligo-attached magnetic beads. After fragmentation, the first strand
662 cDNA was synthesized using random hexamer primers followed by the second strand
663 cDNA synthesis. The library was ready after end repair, A-tailing, adapter ligation, size
664 selection, amplification, and purification.

665 The library was checked with Qubit and real-time PCR for quantification and
666 bioanalyzer for size distribution detection. Libraries were pooled and sequenced in
667 2x150bp paired-end mode on a S4 flowcell in the Illumina Novaseq6000 platform. A
668 minimum of 40 million reads were generated from each library.

669

670 **Bioinformatic analysis of the RNA-seq**

671 RNA-seq analysis were performed as previously described[61] with minor modifications:
672 quality control of the raw data was performed with FastQC (v.0.11.9). RNA-seq reads
673 were mapped to the Mouse genome (GRCm39) using STAR (v2.7.9a)[62] and SAM/BAM
674 files were further processed using SAMtools (v1.15). Aligned reads were counted and
675 assigned to genes using Ensembl release 104 gene annotation and FeatureCounts,
676 Subread (v2.0.1). Normalization of read counts and differential expression analyses
677 were performed using DESeq2 (v1.32)[63], Bioconductor (v3.15)[64] in the R statistical
678 computing and graphics platform (v4.2.2 “Innocent and Trusting”).

679 In the analysis of wpVPM and ulVPM datasets (control and embWPC samples)
680 generated for this study, significantly Differentially Expressed Genes (DEGs) were
681 identified using a simultaneous statistical significance threshold (Benjamini-Hochberg
682 (BH) adjusted *P*-value < 0.1) and absolute log2 fold change (log2FC) > 0.14 by shrunken
683 log2FC using the adaptive *T* prior Bayesian shrinkage estimator “apeglm” (**Tables S1**
684 and **S2**)[65]. Hierarchical clustering analysis was performed using “Euclidean” distance
685 and “Complete” clustering methods metrics to visualize significantly upregulated and

686 down-regulated genes. A linear support-vector machine (SVM) model for classifying
687 RNA-seq samples was developed using the e1071 package (v1.7-14). This model was
688 based on the gene expression profiles of the top 500 most variable genes in ulVPM and
689 wpVPM control samples. Subsequently, the C-SVM model was utilized to predict the
690 classification of ulVPM embWPC samples based on their transcriptomic profiles.

691 Functional enrichment analyses were performed using clusterProfiler (v4.4.4)[66]
692 under org.Mm.eg.db package (v3.15) for better annotation data. All enriched terms were
693 considered significant at adjusted P-values by 'BH' < 0.1, in the Gene Ontology (GO)
694 Over-Representation Analysis. Enrichment results were further clustered and simplified
695 using the simplifyEnrichment package (version 1.11.1)[67] (**Table S3**).

696

697 ***Ex vivo* calcium imaging**

698 At E16, embryos were retrieved from the dam's uterus by cesarean section, their brains
699 were rapidly dissected out and they were submerged in an ice-cold slicing solution
700 containing (in mM): 2.5 KCl, 7 $MgSO_4$, 0.5 $CaCl_2$, 1 NaH_2PO_4, 26 Na_2HCO_3, 11 glucose
701 and 228 sucrose. Coronal slices (350 μm thick) were obtained using a vibratome
702 (VT1200S Leica) and they were left to recover for at least 30 minutes at room
703 temperature in standard artificial cerebrospinal fluid (ACSF) containing (in mM): 119
704 NaCl, 5 KCl, 1.3 $MgSO_4$, 2.4 $CaCl_2$, 1 NaH_2PO_4, 26 Na_2HCO_3 and 11 glucose. All
705 extracellular solutions were continuously bubbled with a 95% O_2 and 5% CO_2 gas
706 mixture. Slices were loaded with the calcium indicator Cal520TM (AAT Bioquest) as
707 previously described[10,21], transferred to a submersion-type recording chamber and
708 perfused with warm ACSF (32-34 ºC) at a rate of 1.8 ml/min. Images were acquired with
709 a digital charge-coupled device (CCD) camera (ORCA-R2 C10600-10B, Hamamatsu)
710 coupled to an upright microscope (DM-LFSA, Leica) and using a 5x objective. For
711 recordings of spontaneous calcium activity, frames were acquired with an exposure time
712 of 150 ms, an interframe interval of 300 ms, a frame size of 672x512 pixel and a spatial

713 resolution of 2.5 μm/pixel. With each slice, 1 to 5 epochs of 15 mins (3000 frames) were
714 recorded.
715
716 **Analysis of fluorescence spontaneous activity**
717 Analysis of spontaneous thalamic calcium activity was conducted using custom software
718 developed in Matlab™, which was adapted from the CalciumDX toolbox (indexed in the
719 Data and code availability section). For each movie, VPM was delineated, and the two
720 prospective areas (wpVPM and ulVPM) were subdivided into a grid of 6x6 pixels where
721 each small square is a region of interest (ROI). Calcium activity events were detected
722 based on the average calcium signal of each ROI over time, employing threshold-based
723 algorithms modified from CalciumDX. To identify significant synchronous activity and
724 discard ROI co-activation that resulting from random temporal coincidence of calcium
725 events, we generated surrogated calcium events sequences for each experiment using
726 Matlab™. The alternative dataset was built by randomly shuffling the original temporal
727 intervals between calcium transients in every ROI while preserving the spiking frequency
728 and temporal structure of the calcium activity. Subsequently, the maximum value of co-
729 activation from shuffled data was calculated. Through 1000 iterations, we established a
730 synchronicity threshold as the 95th percentile of the maximum values of co-activation
731 obtained from the shuffled dataset. In each experiment, only activity super passing the
732 synchronicity threshold was used for calculations and visualization. The onset of a
733 synchronic event was defined as the frame in which co-activation overpass the threshold,
734 while the end was determined as the frame in which co-activation reached 25% of peak
735 synchronicity.
736
737 **Quantification and statistical analysis**
738 Data were analysed using Prism 9 (GraphPad). A Kolmogorov-Smirnov normality test
739 was conducted on all datasets. For independent data that conforming to a normal
740 distribution, an unpaired two-tailed Student's *t*-test was employed to compare two

741 groups. In cases where independent data that did not follow a normal distribution, a
742 Mann-Whitney *U*-Test two-tailed test was used for comparison. For analyses involving
743 more than two groups and one factor, one-way ANOVA was applied, followed by a Tukey
744 *post hoc* analysis when data exhibited a normal distribution. For more than two groups
745 and two factors, two-way ANOVA was conducted, followed by a Tukey *post hoc* analysis
746 for normally distributed data. When data did not conform to a normal distribution, a
747 Kruskal-Wallis test was performed, followed by Dunn's multiple comparisons without any
748 correction. Results are presented as mean ± standard error of mean (SEM) with the n
749 value for each dataset. Statistically significant effects and n numbers are detailed in the
750 corresponding figure legend or STAR Methods. The significance threshold was set at
751 0.05, two-tailed (not significant, ns, $p > 0.05$; *$p < 0.05$; **$p < 0.01$; ***$p < 0.001$). No data
752 exclusion was performed. Data for RNA-seq were processed according to the description
753 in the STAR Methods sections, and statistical details are explained in the results and
754 corresponding figure legends.
755

756 **References**

757 1. Rakic, P. (1988). Specification of cerebral cortical areas. Science *241*, 170-176.
758 10.1126/science.3291116.
759 2. O'Leary, D.D., and Sahara, S. (2008). Genetic regulation of arealization of the neocortex.
760 Curr Opin Neurobiol *18*, 90-100. 10.1016/j.conb.2008.05.011.
761 3. O'Leary, D.D., Chou, S.J., and Sahara, S. (2007). Area patterning of the mammalian
762 cortex. Neuron *56*, 252-269. 10.1016/j.neuron.2007.10.010.
763 4. Grove, E.A., and Fukuchi-Shimogori, T. (2003). Generating the cerebral cortical area
764 map. Annu Rev Neurosci *26*, 355-380. 10.1146/annurev.neuro.26.041002.131137.
765 5. Harris, K.D., and Shepherd, G.M. (2015). The neocortical circuit: themes and variations.
766 Nat Neurosci *18*, 170-181. 10.1038/nn.3917.
767 6. Welker, C. (1976). Receptive fields of barrels in the somatosensory neocortex of the rat.
768 J Comp Neurol *166*, 173-189. 10.1002/cne.901660205.
769 7. Diamond, M.E., von Heimendahl, M., Knutsen, P.M., Kleinfeld, D., and Ahissar, E.
770 (2008). 'Where' and 'what' in the whisker sensorimotor system. Nat Rev Neurosci *9*, 601-
771 612. 10.1038/nrn2411.
772 8. Brecht, M., Preilowski, B., and Merzenich, M.M. (1997). Functional architecture of the
773 mystacial vibrissae. Behav Brain Res *84*, 81-97. 10.1016/s0166-4328(97)83328-1.
774 9. Woolsey, T.A., and Van der Loos, H. (1970). The structural organization of layer IV in
775 the somatosensory region (SI) of mouse cerebral cortex. The description of a cortical field
776 composed of discrete cytoarchitectonic units. Brain Res *17*, 205-242. 10.1016/0006-
777 8993(70)90079-x.
778 10. Moreno-Juan, V., Filipchuk, A., Anton-Bolanos, N., Mezzera, C., Gezelius, H., Andres,
779 B., Rodriguez-Malmierca, L., Susin, R., Schaad, O., Iwasato, T., et al. (2017). Prenatal

thalamic waves regulate cortical area size prior to sensory processing. Nat Commun *8*, 14172. 10.1038/ncomms14172.

11. Lopez-Bendito, G., Anibal-Martinez, M., and Martini, F.J. (2022). Cross-Modal Plasticity in Brains Deprived of Visual Input Before Vision. Annu Rev Neurosci *45*, 471-489. 10.1146/annurev-neuro-111020-104222.
12. Gaspar, P., and Erzurumlu, R. (2013). The Birth of the Barrels. Developmental Cell *27*, 3-4. 10.1016/j.devcel.2013.09.028.
13. Erzurumlu, R.S., and Gaspar, P. (2020). How the Barrel Cortex Became a Working Model for Developmental Plasticity: A Historical Perspective. The Journal of Neuroscience *40*, 6460-6473. 10.1523/jneurosci.0582-20.2020.
14. Mizuno, H., Luo, W., Tarusawa, E., Saito, Y.M., Sato, T., Yoshimura, Y., Itohara, S., and Iwasato, T. (2014). NMDAR-regulated dynamics of layer 4 neuronal dendrites during thalamocortical reorganization in neonates. Neuron *82*, 365-379. 10.1016/j.neuron.2014.02.026.
15. Laumonnerie, C., Bechara, A., Vilain, N., Kurihara, Y., Kurihara, H., and Rijli, F.M. (2015). Facial whisker pattern is not sufficient to instruct a whisker-related topographic map in the mouse somatosensory brainstem. Development *142*, 3704-3712. 10.1242/dev.128736.
16. Ozdinler, P.H., and Erzurumlu, R.S. (2002). Slit2, a branching-arborization factor for sensory axons in the Mammalian CNS. J Neurosci *22*, 4540-4549. 10.1523/JNEUROSCI.22-11-04540.2002.
17. Oury, F., Murakami, Y., Renaud, J.S., Pasqualetti, M., Charnay, P., Ren, S.Y., and Rijli, F.M. (2006). Hoxa2- and rhombomere-dependent development of the mouse facial somatosensory map. Science *313*, 1408-1413. 10.1126/science.1130042.
18. Kitazawa, T., and Rijli, F.M. (2018). Barrelette map formation in the prenatal mouse brainstem. Curr Opin Neurobiol *53*, 210-219. 10.1016/j.conb.2018.09.008.
19. Bechara, A., Laumonnerie, C., Vilain, N., Kratochwil, C.F., Cankovic, V., Maiorano, N.A., Kirschmann, M.A., Ducret, S., and Rijli, F.M. (2015). Hoxa2 Selects Barrelette Neuron Identity and Connectivity in the Mouse Somatosensory Brainstem. Cell Rep *13*, 783-797. 10.1016/j.celrep.2015.09.031.
20. Zembrzycki, A., Chou, S.J., Ashery-Padan, R., Stoykova, A., and O'Leary, D.D. (2013). Sensory cortex limits cortical maps and drives top-down plasticity in thalamocortical circuits. Nat Neurosci *16*, 1060-1067. 10.1038/nn.3454.
21. Anton-Bolanos, N., Sempere-Ferrandez, A., Guillamon-Vivancos, T., Martini, F.J., Perez-Saiz, L., Gezelius, H., Filipchuk, A., Valdeolmillos, M., and Lopez-Bendito, G. (2019). Prenatal activity from thalamic neurons governs the emergence of functional cortical maps in mice. Science *364*, 987-990. 10.1126/science.aav7617.
22. Guillamon-Vivancos, T., Anibal-Martinez, M., Puche-Aroca, L., Moreno-Bravo, J.A., Valdeolmillos, M., Martini, F.J., and Lopez-Bendito, G. (2022). Input-dependent segregation of visual and somatosensory circuits in the mouse superior colliculus. Science *377*, 845-850. 10.1126/science.abq2960.
23. Frangeul, L., Pouchelon, G., Telley, L., Lefort, S., Luscher, C., and Jabaudon, D. (2016). A cross-modal genetic framework for the development and plasticity of sensory pathways. Nature *538*, 96-98. 10.1038/nature19770.
24. Gezelius, H., and Lopez-Bendito, G. (2017). Thalamic neuronal specification and early circuit formation. Dev Neurobiol *77*, 830-843. 10.1002/dneu.22460.
25. Ono, K., Clavairoly, A., Nomura, T., Gotoh, H., Uno, A., Armant, O., Takebayashi, H., Zhang, Q., Shimamura, K., Itohara, S., et al. (2014). Development of the prethalamus is crucial for thalamocortical projection formation and is regulated by Olig2. Development *141*, 2075-2084. 10.1242/dev.097790.
26. Vitalis, T., Dauphinot, L., Gressens, P., Potier, M.C., Mariani, J., and Gaspar, P. (2018). RORalpha Coordinates Thalamic and Cortical Maturation to Instruct Barrel Cortex Development. Cereb Cortex *28*, 3994-4007. 10.1093/cercor/bhx262.

27. Rubenstein, J., Anderson, S., Shi, L., Miyashita-Lin, E., Bulfone, A., and Hevner, R. (1999). Genetic control of cortical regionalization and connectivity. Cereb Cortex *9*, 524-532.
28. Mercurio, S., Serra, L., Motta, A., Gesuita, L., Sanchez-Arrones, L., Inverardi, F., Foglio, B., Barone, C., Kaimakis, P., Martynoga, B., et al. (2019). Sox2 Acts in Thalamic Neurons to Control the Development of Retina-Thalamus-Cortex Connectivity. iScience *15*, 257-273. 10.1016/j.isci.2019.04.030.
29. Nakagawa, Y., and O'Leary, D.D. (2003). Dynamic patterned expression of orphan nuclear receptor genes RORalpha and RORbeta in developing mouse forebrain. Dev Neurosci *25*, 234-244. 10.1159/000072271.
30. Yuge, K., Kataoka, A., Yoshida, A.C., Itoh, D., Aggarwal, M., Mori, S., Blackshaw, S., and Shimogori, T. (2011). Region-specific gene expression in early postnatal mouse thalamus. J Comp Neurol *519*, 544-561. 10.1002/cne.22532.
31. Ebisu, H., Iwai-Takekoshi, L., Fujita-Jimbo, E., Momoi, T., and Kawasaki, H. (2017). Foxp2 Regulates Identities and Projection Patterns of Thalamic Nuclei During Development. Cereb Cortex *27*, 3648-3659. 10.1093/cercor/bhw187.
32. Puelles, L., Sanchez, M.P., Spreafico, R., and Fairen, A. (1992). Prenatal development of calbindin immunoreactivity in the dorsal thalamus of the rat. Neuroscience *46*, 135-147. 10.1016/0306-4522(92)90013-r.
33. Dufour, A., Seibt, J., Passante, L., Depaepe, V., Ciossek, T., Frisen, J., Kullander, K., Flanagan, J., Polleux, F., and Vanderhaeghen, P. (2003). Area specificity and topography of thalamocortical projections are controlled by ephrin/Eph genes. Neuron *39*, 453-465. S0896627303004409 [pii].
34. Shigematsu, N., Miyamoto, Y., Esumi, S., and Fukuda, T. (2024). The Anterolateral Barrel Subfield Differs from the Posteromedial Barrel Subfield in the Morphology and Cell Density of Parvalbumin-Positive GABAergic Interneurons. eNeuro *11*. 10.1523/ENEURO.0518-22.2024.
35. Killackey, H.P., and Dawson, D.R. (1989). Expansion of the Central Hindpaw Representation Following Fetal Forelimb Removal in the Rat. Eur J Neurosci *1*, 210-221. 10.1111/j.1460-9568.1989.tb00790.x.
36. Van der Loos, H., and Woolsey, T.A. (1973). Somatosensory cortex: structural alterations following early injury to sense organs. Science *179*, 395-398. 10.1126/science.179.4071.395.
37. Killackey, H.P., and Belford, G.R. (1979). The formation of afferent patterns in the somatosensory cortex of the neonatal rat. J Comp Neurol *183*, 285-303. 10.1002/cne.901830206.
38. Woolsey, T.A., Anderson, J.R., Wann, J.R., and Stanfield, B.B. (1979). Effects of early vibrissae damage on neurons in the ventrobasal (VB) thalamus of the mouse. J Comp Neurol *184*, 363-380. 10.1002/cne.901840210.
39. Belford, G.R., and Killackey, H.P. (1979). The development of vibrissae representation in subcortical trigeminal centers of the neonatal rat. J Comp Neurol *188*, 63-74. 10.1002/cne.901880106.
40. Woolsey, T.A., and Wann, J.R. (1976). Areal changes in mouse cortical barrels following vibrissal damage at different postnatal ages. J Comp Neurol *170*, 53-66. 10.1002/cne.901700105.
41. Killackey, H.P., Belford, G., Ryugo, R., and Ryugo, D.K. (1976). Anomalous organization of thalamocortical projections consequent to vibrissae removal in the newborn rat and mouse. Brain Res *104*, 309-315. 10.1016/0006-8993(76)90623-5.
42. Renier, N., Dominici, C., Erzurumlu, R.S., Kratochwil, C.F., Rijli, F.M., Gaspar, P., and Chedotal, A. (2017). A mutant with bilateral whisker to barrel inputs unveils somatosensory mapping rules in the cerebral cortex. Elife *6*. 10.7554/eLife.23494.
43. Belford, G.R., and Killackey, H.P. (1980). The sensitive period in the development of the trigeminal system of the neonatal rat. J Comp Neurol *193*, 335-350. 10.1002/cne.901930203.

44. Martini, F.J., Guillamon-Vivancos, T., Moreno-Juan, V., Valdeolmillos, M., and Lopez-Bendito, G. (2021). Spontaneous activity in developing thalamic and cortical sensory networks. Neuron *109*, 2519-2534. 10.1016/j.neuron.2021.06.026.
45. Mire, E., Mezzera, C., Leyva-Díaz, E., Paternain, A.V., Squarzoni, P., Bluy, L., Castillo-Paterna, M., López, M.J., Peregrín, S., Tessier-Lavigne, M., et al. (2012). Spontaneous activity regulates Robo1 transcription to mediate a switch in thalamocortical axon growth. Nat Neurosci *15*, 1134-1143. 10.1038/nn.3160.
46. Land, P.W., and Simons, D.J. (1985). Cytochrome oxidase staining in the rat SmI barrel cortex. J Comp Neurol *238*, 225-235. 10.1002/cne.902380209.
47. Jan, T.A., Lu, L., Li, C.X., Williams, R.W., and Waters, R.S. (2008). Genetic analysis of posterior medial barrel subfield (PMBSF) size in somatosensory cortex (SI) in recombinant inbred strains of mice. BMC Neurosci *9*, 3. 10.1186/1471-2202-9-3.
48. Kleinfeld, D., Ahissar, E., and Diamond, M.E. (2006). Active sensation: insights from the rodent vibrissa sensorimotor system. Curr Opin Neurobiol *16*, 435-444. 10.1016/j.conb.2006.06.009.
49. Grant, R.A., Sperber, A.L., and Prescott, T.J. (2012). The role of orienting in vibrissal touch sensing. Front Behav Neurosci *6*, 39. 10.3389/fnbeh.2012.00039.
50. Kuruppath, P., Gugig, E., and Azouz, R. (2014). Microvibrissae-based texture discrimination. J Neurosci *34*, 5115-5120. 10.1523/JNEUROSCI.4217-13.2014.
51. Morita, T., Kang, H., Wolfe, J., Jadhav, S.P., and Feldman, D.E. (2011). Psychometric curve and behavioral strategies for whisker-based texture discrimination in rats. PLoS One *6*, e20437. 10.1371/journal.pone.0020437.
52. Gorski, J.A., Talley, T., Qiu, M., Puelles, L., Rubenstein, J.L., and Jones, K.R. (2002). Cortical excitatory neurons and glia, but not GABAergic neurons, are produced in the Emx1-expressing lineage. J Neurosci *22*, 6309-6314. 10.1523/JNEUROSCI.22-15-06309.2002.
53. Chen, L., Guo, Q., and Li, J. (2009). Transcription factor Gbx2 acts cell-nonautonomously to regulate the formation of lineage-restriction boundaries of the thalamus. Development *136*, 1317-1326. 10.1242/dev.030510.
54. Franco, S.J., Gil-Sanz, C., Martinez-Garay, I., Espinosa, A., Harkins-Perry, S.R., Ramos, C., and Muller, U. (2012). Fate-restricted neural progenitors in the mammalian cerebral cortex. Science *337*, 746-749. 10.1126/science.1223616.
55. Voiculescu, O., Charnay, P., and Schneider-Maunoury, S. (2000). Expression pattern of a Krox-20/Cre knock-in allele in the developing hindbrain, bones, and peripheral nervous system. Genesis *26*, 123-126. 10.1002/(sici)1526-968x(200002)26:2<123::aid-gene7>3.0.co;2-o.
56. Madisen, L., Garner, A.R., Shimaoka, D., Chuong, A.S., Klapoetke, N.C., Li, L., van der Bourg, A., Niino, Y., Egolf, L., Monetti, C., et al. (2015). Transgenic mice for intersectional targeting of neural sensors and effectors with high specificity and performance. Neuron *85*, 942-958. 10.1016/j.neuron.2015.02.022.
57. Renier, N., Wu, Z., Simon, D.J., Yang, J., Ariel, P., and Tessier-Lavigne, M. (2014). iDISCO: a simple, rapid method to immunolabel large tissue samples for volume imaging. Cell *159*, 896-910. 10.1016/j.cell.2014.10.010.
58. Renier, N., Adams, E.L., Kirst, C., Wu, Z., Azevedo, R., Kohl, J., Autry, A.E., Kadiri, L., Umadevi Venkataraju, K., Zhou, Y., et al. (2016). Mapping of Brain Activity by Automated Volume Analysis of Immediate Early Genes. Cell *165*, 1789-1802. 10.1016/j.cell.2016.05.007.
59. Madisen, L., Zwingman, T.A., Sunkin, S.M., Oh, S.W., Zariwala, H.A., Gu, H., Ng, L.L., Palmiter, R.D., Hawrylycz, M.J., Jones, A.R., et al. (2010). A robust and high-throughput Cre reporting and characterization system for the whole mouse brain. Nat Neurosci *13*, 133-140. 10.1038/nn.2467.
60. James B. Ackman, H.Z., Michael C. Crair (2014). Structured dynamics of neural activity across developing neocortex. Preprint at bioRxiv. 10.1101/012237.
61. Herrero-Navarro, A., Puche-Aroca, L., Moreno-Juan, V., Sempere-Ferrandez, A., Espinosa, A., Susin, R., Torres-Masjoan, L., Leyva-Diaz, E., Karow, M., Figueres-Onate,

M., et al. (2021). Astrocytes and neurons share region-specific transcriptional signatures that confer regional identity to neuronal reprogramming. Sci Adv *7*. 10.1126/sciadv.abe8978.
62. Dobin, A., Davis, C.A., Schlesinger, F., Drenkow, J., Zaleski, C., Jha, S., Batut, P., Chaisson, M., and Gingeras, T.R. (2013). STAR: ultrafast universal RNA-seq aligner. Bioinformatics *29*, 15-21. 10.1093/bioinformatics/bts635.
63. Love, M.I., Huber, W., and Anders, S. (2014). Moderated estimation of fold change and dispersion for RNA-seq data with DESeq2. Genome Biol *15*, 550. 10.1186/s13059-014-0550-8.
64. Huber, W., Carey, V.J., Gentleman, R., Anders, S., Carlson, M., Carvalho, B.S., Bravo, H.C., Davis, S., Gatto, L., Girke, T., et al. (2015). Orchestrating high-throughput genomic analysis with Bioconductor. Nat Methods *12*, 115-121. 10.1038/nmeth.3252.
65. Zhu, A., Srivastava, A., Ibrahim, J.G., Patro, R., and Love, M.I. (2019). Nonparametric expression analysis using inferential replicate counts. Nucleic Acids Res *47*, e105. 10.1093/nar/gkz622.
66. Gu, Z., and Hubschmann, D. (2023). simplifyEnrichment: A Bioconductor Package for Clustering and Visualizing Functional Enrichment Results. Genomics Proteomics Bioinformatics *21*, 190-202. 10.1016/j.gpb.2022.04.008.
67. Yu, G., Wang, L.G., Han, Y., and He, Q.Y. (2012). clusterProfiler: an R package for comparing biological themes among gene clusters. OMICS *16*, 284-287. 10.1089/omi.2011.0118.

Acknowledgements

We thank Belén Andrés and María Aurelia Torregrosa for their technical support. We thank Teresa Guillamón-Vivancos and Miguel Valdeolmillos for their comments and input on the manuscript and other members of López-Bendito's laboratory for stimulating discussions. This work was supported by grants from the Swiss National Science Foundation (31003A_175776 and 310030_219370) and the Novartis Research Foundation to F.M.R., and by grants from the European Research Council (ERC) under the European Union's Horizon 2020 research and innovation programme (ERC-2021-ADG-101054313 SPONTSENSE), PID2021-127112NB-I00 from the MCIN/AEI /10.13039/501100011033/ and ERDF A way to make Europe, and Generalitat Valenciana, Conselleria d'Educació, Universitats, i Ocupació (PROMETEO 2021/052) to G.L.-B.

Author contributions

Conceptualization, M.A-M. and G.L-B.; methodology, M.A-M., G.P., MP.M. and LM.R-M; data curation, M.A-M., G.P., MP.M. and L.P.; transcriptomic analysis, L.P.; writing –

original draft, M.A-M., and G.L-B.; writing – review & editing, M.A-M., L.P., G.P., FJ.M., FM.R., and G.L-B.; funding acquisition, FM.R., and G.L-B.; resources, FM.R., and G.L-B.; supervision, FJ.M., FM.R., and G.L-B.

Competing interests

The authors declare no competing interests.

Declaration of generative AI and AI-assisted technologies in the writing process

During the preparation of this work the authors used Chat-GPT in order to streamline some parts of the text. After using this tool, the authors reviewed and edited the content as needed and take full responsibility for the content of the publication.

Resource Availability

Lead contact

Additional information and requests for resources and reagents should be directed to the lead contact, Guillermina López-Bendito (g.lbendito@umh.es).

Materials availability

This study did not generate new mouse lines.

This study did not generate new unique reagents.

Figures

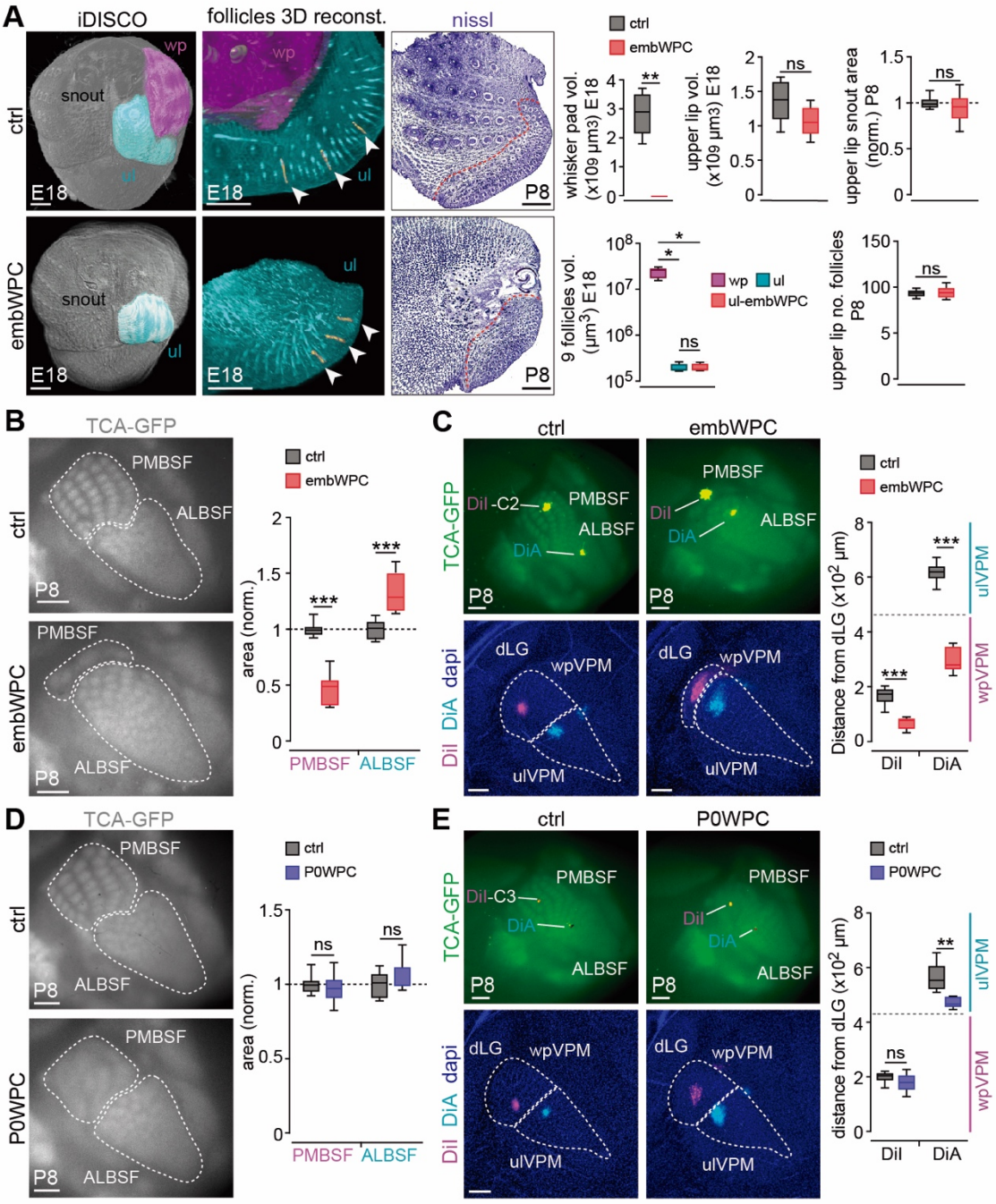

Figure 1. Whisker pad deprivation in embryos rescales barrel field areas and thalamocortical circuits. (A) Left and middle, iDISCO frontal snout views showing the whisker pad (magenta) and upper lip (cyan) areas, and lateral 3D-reconstructions of the follicles (yellow) of the snout at E18 in control and after whisker pad cauterization of the mystacial whiskers mice. Right, Nissl stainings of the snout at P8 in control and embWPC mice, red dashed line delimits upper lip area. Quantification of the data (iDISCO E18, n= 5 ctrl mice, n= 5 embWPC mice, whisker pad volume, unpaired two-tailed Student *t*-test; upper lip volume, unpaired two-tailed Student *t*-test. ns, p= 0.11; upper lip area, unpaired

1016 two-tailed Student *t*-test. ns, p= 0.32; upper lip 9 follicles volume, Mann-Whitney *U*-test.
1017 ns, p= 0.73. Nissl P8, n= 8 ctrl mice, n= 9 embWPC mice; upper lip number of follicles,
1018 unpaired two-tailed Student *t*-test. ns, p= 0.78). **(B)** Surface view of thalamocortical
1019 terminals (TCA-GFP+) in the cortical PMBSF and ALBSF in control and embWPC mice
1020 at P8. Quantification of the data (n= 8 ctrl mice, n= 9 embWPC mice, unpaired two-tailed
1021 Student *t*-test). **(C)** Upper panels, DiI and DiA crystal placements in the C2 cortical barrel
1022 and in the ALBSF, respectively, in control and embWPC at P8. Lower panels,
1023 backlabelled cells at the level of the wpVPM and ulVPM showing the relative
1024 displacement of the labelling in embWPC mice. Quantification of the position of
1025 backlabelled cells with respect to the distance to the dLG nucleus. The gray horizontal
1026 dashed line in the graph represents the separation between wpVPM and ulVPM (n= 6
1027 ctrl mice, n= 6 embWPC mice, unpaired two-tailed Student *t*-test). **(D)** Surface view of
1028 thalamocortical terminals (TCA-GFP+) in the cortical PMBSF and ALBSF in control and
1029 P0WPC mice at P8. Quantification of the data (n= 8 ctrl mice, n= 9 P0PC mice, unpaired
1030 two-tailed Student *t*-test. ns, PMBSF, p= 0.55, ALBSF, p= 0.30). **(E)** Upper panels, DiI
1031 and DiA crystal placements in the C3 cortical barrel and in the ALBSF, respectively, in
1032 control and P0WPC at P8. Lower panels, backlabelled cells at the level of the wpVPM
1033 and ulVPM. Quantification of the position of backlabelled cells with respect to the
1034 distance to the dLG nucleus. The gray horizontal dashed line in the graph represents the
1035 separation between wpVPM and ulVPM (n= 5 ctrl mice, n= 5 P0WPC mice, unpaired
1036 two-tailed Student *t*-test. ns, p= 0.09). wp, whisker pad; ul, upper lip; E, embryonic; P,
1037 postnatal; embWPC, embryonic whisker pad cauterized; P0WPC, postnatal day 0
1038 whisker pad cauterized; vol., volume; no., number; TCA-GFP, thalamocortical axons
1039 labelled with green fluorescent protein; PMBSF, postero-medial barrel subfield; ALBSF,
1040 antero-lateral barrel subfield; wpVPM, whisker pad recipient ventral posteromedial
1041 nucleus; ulVPM, upper lip recipient ventral posteromedial nucleus; norm., normalized.
1042 Scale bars, (A, left) 500 μm; (A, middle) 400 μm; (A, right) 1000 μm; (B), (C, top), (D)
1043 and (E, top) 500 μm; (C, bottom) and (E, bottom) 200 μm. Boxplots show the medians
1044 with the interquartile range (box) and range (whiskers). Bar graphs show the means ±
1045 SEM. ns, not significant. *p < 0.05, **p < 0.01, ***p < 0.001. See also Figures S1-S5;
1046 Videos S1 and S2.

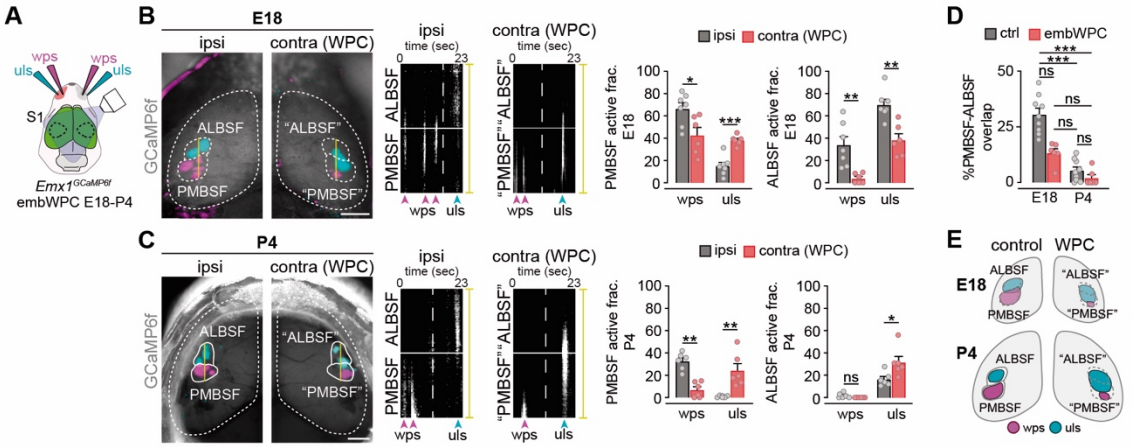

Figure 2. Functional rescaling of cortical barrel field territories in embWPC mice. **(A)** Schema representing the experimental paradigm. **(B)** Left, cortical evoked responses (GCaMP6f) to whisker pad (magenta) and upper lip (cyan) stimulations in control (ipsilateral) and whisker pad cauterized (WPC, contralateral) sides in embWPC mice at E18. Control PMBSF and ALBSF territories were translated to the WPC side for direct comparison and labelled as "PMBSF" and "ALBSF". Right, reslice of the yellow line in the left, representing responses elicited in PMBSF and ALBSF primordia by whisker pad stimulation (wps) or upper lip stimulations (uls). The white horizontal line delineates the boundaries between PMBSF and ALBSF, while the vertical dashed line divides the wps from the uls over time. Quantification of the PMBSF and ALBSF active fraction to wps or uls (n= 7 ctrl, n= 6 WPC, unpaired two-tailed Student *t*-test). **(C)** Left, cortical evoked responses (GCaMP6f) to whisker pad (magenta) and upper lip (cyan) stimulations in control (ipsilateral) and WPC (contralateral) sides in embWPC at P4. Right, reslice of the yellow line in the left, representing responses elicited in PMBSF or ALBSF by wps or uls. The white horizontal line delineates the boundaries between PMBSF and ALBSF, while the vertical dashed line divides the wps from the uls over time. Quantification of the PMBSF and ALBSF active fraction to wps and uls (n= 6 ctrl side, n= 6 WPC side, PMBSF active fraction, unpaired two-tailed Student *t*-test; ALBSF active fraction, Mann-Whitney *U*-test. ns, p= 0.06). **(D)** Quantification of the percentage of overlap responses between the PMBSF and ALBSF territories at E18 and P4 (n= 9 ctrl mice E18, n= 6 embWPC mice E18, n= 9 ctrl mice P4, n= 6 embWPC mice P4, Kruskal-Wallis test, ***p <0.001. Dunn's multiple comparison test post-hoc analysis, ctrl E18 vs embwpc E18 ns, p= 0.37; embWPC E18 vs ctrl P4 ns, p= 0.77; embWPC E18 vs embWPC P4 ns, p= 0.14; ctrl P4 vs embWPC P4 ns, p > 0.99). **(E)** Schema illustrating the results found. Dashed lines delineate PMBSF and ALBSF putative evoked territories at E18. S1, primary somatosensory cortex; wps, whisker pad stimulation; uls, upper lip stimulation; GCaMP6f, calmodulin-based genetically encoded fluorescent calcium indicator 6–fast; WPC, whisker pad cauterized; contra, contralateral cortex to the whisker pad cauterized; ipsi, ipsilateral cortex to the whisker pad cauterized. Scale bars, 1000 μm. Bar graphs show the means ± SEM. ns, not significant. *p < 0.05, **p < 0.01, ***p < 0.001. See also Videos S3-S6.

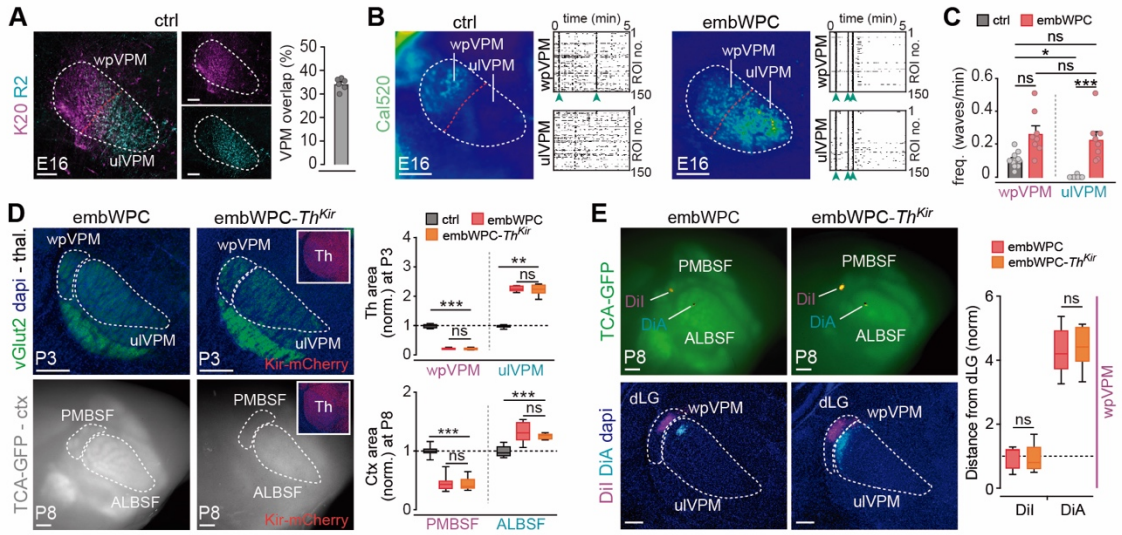

Figure 3. ALBSF rescaling is independent of thalamic patterned activity. (A) Coronal sections from the *Krox20-zsgreen::R2-mCherry* double transgenic mouse showing Krox20-labelled axons (magenta, vPrV) and R2-labelled axons (cyan, dPrV) at the VPM of the thalamus at E16. Quantification of the percentage of overlap of labelled axons at the thalamus (n= 6). **(B)** Maximal projection of *ex vivo* spontaneous calcium activity in the prospective VPM sub-regions (wpVPM and ulVPM) of the thalamus in acute slices at E16. Raster plots of 5 minutes. **(C)** Quantification of the frequency of waves activity in the VPM in both control and embWPC mice (n= 11 ctrl mice, n= 8 embWPC mice, Kruskal-Wallis test, ***p <0.001. Dunn's multiple comparison test post-hoc analysis, prospective wpVPM ctrl vs prospective wpVPM embWPC ns, p= 0.14; prospective wpVPM ctrl vs prospective ulVPM embWPC ns, p= 0.32; prospective wpVPM embWPC vs prospective ulVPM embWPC ns, p >0.99). **(D)** Upper panels, coronal sections of vGlut2 staining (green) showing the size of the wpVPM and ulVPM in the thalamus of embWPC and embWPC-*Th*^{Kir} mouse (Kir-mCherry positive) at P3. Lower panels, surface view of thalamocortical terminals (TCA-GFP+) in the cortical PMBSF and ALBSF in embWPC and embWPC-*Th*^{Kir} mice at P8. Quantification of the data (Thalamus, n= 5 ctrl mice, n= 5 embWPC mice, n= 6 embWPC-*Th*^{Kir} mice, wpVPM, Two-way ANOVA test: ***p <0.001. Tukey's multiple comparison test post-hoc analysis, ns, p= 0.98; ulVPM, Kruskal-Wallis test, **p <0.01. Dunn's multiple comparison test post-hoc analysis, ns, p >0.99. Cortex, n= 10 ctrl mice, n= 13 embWPC mice, n= 7 embWPC-*Th*^{Kir} mice, PMBSF, Two-way ANOVA test: ***p <0.001. Tukey's multiple comparison test post-hoc analysis, ns, p= 0.99; ALBSF, Two-way ANOVA test: ***p <0.001. Tukey's multiple comparison test post-hoc analysis, ns, p= 0.52). **(E)** Upper panels, DiI and DiA crystal placements in the cortical PMBSF and ALBSF areas, respectively. Lower panels, backlabelled cells at the thalamus show shifted positions within the ulVPM thalamic area in both embWPC and embWPC-*Th*^{Kir} mice at P8. Quantification of the position of backlabelled cells with respect to the distance to the dLG nucleus (n= 6 embWPC mice, n= 6 embWPC-*Th*^{Kir} mice, DiI, Mann-Whitney *U*-test. ns, p= 0.7. DiA, unpaired two-tailed Student *t*-test; ns, 0.76). Scale bars, (A) 100 μm; (B) and (E, bottom) 200 μm; (D, top) 250 μm, (D, bottom) and (E, top) 500 μm. Boxplots show the medians with the interquartile range (box) and range (whiskers). Bar graphs show the means ± SEM. ns, not significant. *p < 0.05, **p < 0.01, ***p < 0.001. See also Figure S6 and S7; Videos S7 and S8.

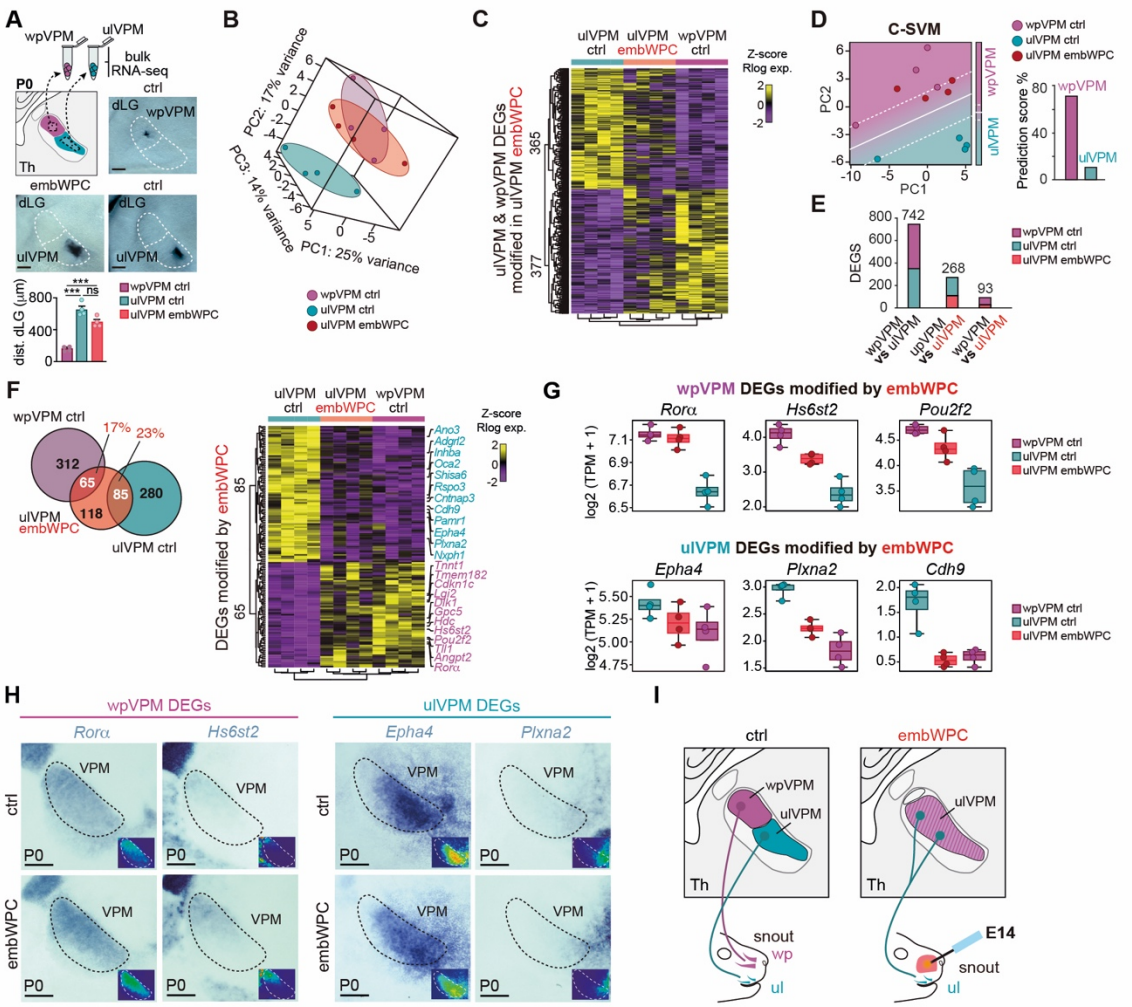

Figure 4. Upper-lip recipient thalamic neurons switch their transcriptional program to that of whisker-pad neurons. (A) Top left, schema representing the experimental paradigm used. Top right and bottom, coronal images showing the dissected thalamic territories for sequencing in control and embWPC slices. Quantification of the dissected area with respect to the distance to the dLG nucleus (n= 4 wpVPM ctrl slices from 4 mice, n= 4 ulVPM ctrl slices from 4 mice, and n= 4 ulWPC embWPC slices from 4 mice, One-way ANOVA test: ***p <0.001. Tukey's multiple comparison test post-hoc analysis, ns, p > 0.05, ***p <0.001). **(B)** Principal Component Analysis (PCA) of wpVPM control (n= 4), ulVPM control (n= 4) and ulVPM whisker pad cauterization (embWPC, n= 4) at P0. **(C)** Heatmap of the normalized regularized logarithm (Rlog) Z-score of expression and unbiased clustering of region-specific DEGs showing their expression profiled in the ulVPM of the embWPC at P0. The color-code (yellow, high expression; purple, low expression) corresponds to the log2FC. **(D)** Left, C-support vector machine (C-SVM) analysis identifies the optimal demarcation plane between wpVPM (magenta dots) and ulVPM population (cyan dots). The ulVPM embWPC samples are identified as wpVPM control based on its gene expression pattern (red dots). Right, Prediction score value of ulVPM embWPC classified as wpVPM (70%) or ulVPM (30%) controls. **(E)** Number of Differentially Expressed Genes (DEGs) obtained in their respective differential expression analysis. **(F)** Left, Venn Diagram shows the number of genes modified by embWPC in ulVPM overlapped in every subset of region specific DEGs. Right, Heatmap

1136 of the normalized regularized logarithm (Rlog) Z-score of expression and unbiased
1137 clustering of region-specific DEGs whose expression was modified by embWPC in the
1138 ulVPM at P0. The color-code (yellow, high expression; purple, low expression)
1139 corresponds to the log2FC. **(G)** Boxplots showing TPM expression levels of selected
1140 wpVPM-specific and ulVPM-specific DEGs modified by embWPC in the ulVPM. Boxplots
1141 show the medians with the interquartile range (box) and range (whiskers). **(H)** Coronal
1142 sections showing by in situ hybridization the change in the pattern of expression of
1143 wpVPM and ulVPM DEGS in the embWPC mouse at P0 (n= 5 ctrl, n= 5 embWPC, for
1144 each probe). **(I)** Schema illustrating the results found. VPM, ventroposterior medial
1145 nucleus. Scale bars, 200 μm. See also Figures S8 and S9.

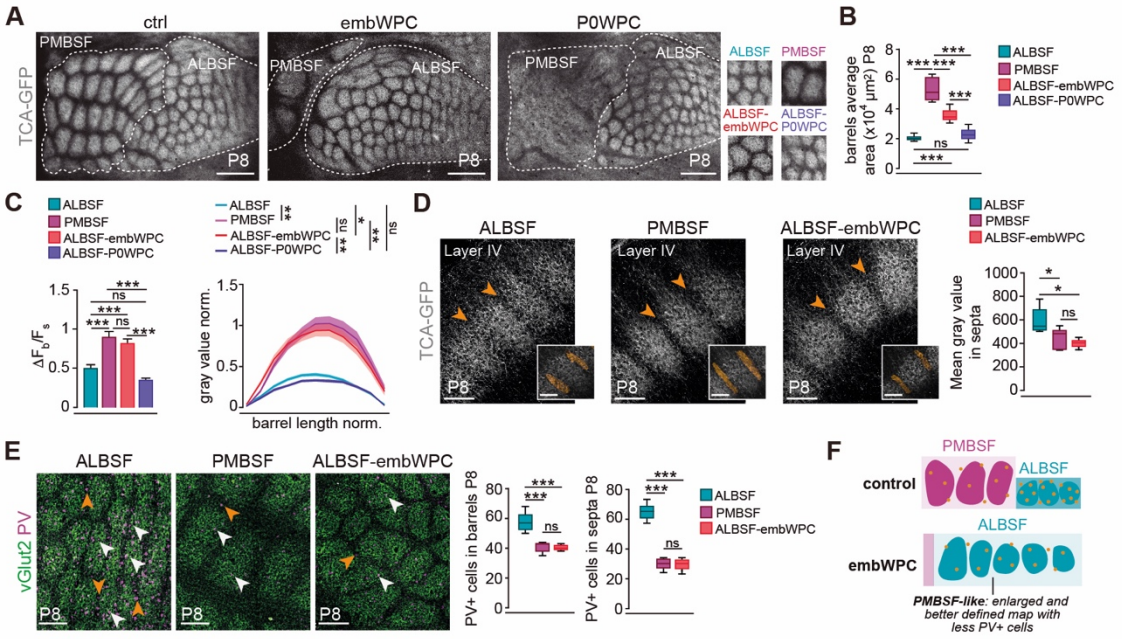

Figure 5. ALBSF barrels acquire PMBSF cortical features. (A) Left, cortical flattened tangential sections showing thalamocortical terminals (TCA-GFP+) in the PMBSF and ALBSF in control, embWPC and P0WPC mice at P8. Right, insets show in detail the clustering of thalamocortical axons in each condition. **(B)** Quantification of the data (barrel average area of 34 barrels, n= 7 ctrl mice PMBSF, n= 9 ctrl mice ALBSF, n= 9 embWPC mice ALBSF, n= 5 P0WPC mice ALBSF, Two-way ANOVA test: ***p <0.001. Tukey's multiple comparison test post-hoc analysis, ns, p= 0.88). **(C)** Left, quantification of the barrel/septum fluorescence ratio (ΔFb/Fs) (n= 12 ctrl mice PMBSF, n= 13 ctrl mice ALBSF, n= 13 embWPC mice ALBSF, n= 5 P0WPC mice ALBSF, Two-way ANOVA test: ***p <0.001. Tukey's multiple comparison test post-hoc analysis, PMBSF-ctrl vs ALBSF-embWPC ns, p= 0.80; ALBSF-ctrl vs ALBSF-P0WPC ns, p= 0.35). Right, quantification of the gray value fluorescence intensity in a barrel (n= 66 ctrl PMBSF barrels, n= 65 ctrl ALBSF barrels, n= 42 embWPC ALBSF barrels, n= 25 P0WPC ALBSF barrels, One-way ANOVA test: ***p <0.001. Tukey's multiple comparison test post-hoc analysis, ns, p= 0.99). **(D)** Coronal sections showing thalamocortical terminals in layer IV in the ALBSF and PMBSF of control, and ALBSF of embWPC mice. Insets showing the septa volume analyzed. Imaris quantification of the EGFP expression from TCA in septa of three barrels per animal (orange arrowheads) (n= 5 ctrl mice ALBSF, n= 5 ctrl mice PMBSF, n= 5 embWPC mice ALBSF, One-way ANOVA test: *p <0.05. Tukey's multiple comparison test post-hoc analysis, ns, p= 0.75). **(E)** Cortical flattened tangential sections showing thalamocortical terminals (vGlut2+) and parvalbumin (PV) expression in barrel core (white arrowheads) and septa (orange arrowheads) in the ALBSF and PMBSF of control, and ALBSF of embWPC mice at P8. Quantification of PV+ cells in 4 barrels and each septa (n= 5 ctrl mice ALBSF, n= 5 ctrl mice PMBSF, n= 5 embWPC mice ALBSF, One-way ANOVA test: ***p <0.001. Tukey's multiple comparison test post-hoc analysis, ns, p >0.05). **(F)** Schema illustrating the results found. Scale bars, (A) 500 µm, (D) 100 µm, (D, insets) 80 µm and (E) 200 µm. Boxplots show the medians with the interquartile range (box) and range (whiskers). Bar graphs show the means ± SEM. ns, not significant. *p < 0.05, **p < 0.01, ***p < 0.001.

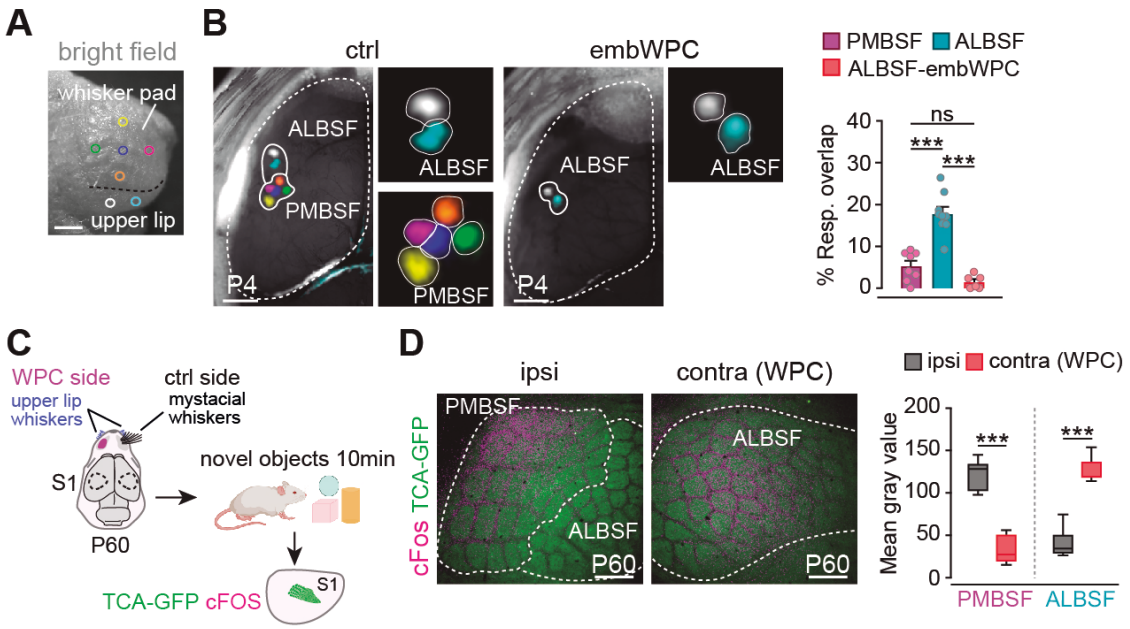

Figure 6. Enhance ALBSF functional map in the postnatal embWPC mice. (A) Schema representing the experimental paradigm. **(B)** Left, cortical evoked responses (GCaMP6f) to five distinct whisker pad stimulations and two distinct upper lip stimulations in control and embWPC mice at P4. Dashed lines indicate the territory covered by elicited responses within the PMBSF and ALBSF. Right, quantification of the percentage of overlap between two distinct PMBSF and two distinct ALBSF responses at P4 (n= 8 ctrl mice for PMBSF responses, n= 9 ctrl mice for ALBSF responses, n= 6 embWPC mice for ALBSF responses, Kruskal-Wallis test, ***p <0.001. Dunn's multiple comparison test post-hoc analysis, ns, p= 0.18). **(C)** Schema representing the experimental paradigm. **(D)** Cortical flattened tangential sections showing thalamocortical terminals (TCA-GFP mouse) and cFOS expression in cortical ipsilateral (control) and contralateral (WPC) sides of P60 mice. Quantification of the mean gray value of cFOS expression in PMBSF and ALBSF in both sides (n= 8 embWPC mice ipsi PMBSF, n= 8 embWPC mice ipsi ALBSF, n= 8 embWPC mice contra (WPC) PMBSF, n= 8 embWPC mice contra (WPC) ALBSF, PMBSF, unpaired two-tailed Student *t*-test; ***p <0.001; ALBSF, Mann-Whitney *U*-test). Scale bars, (A) 1000 μm and (D) 500 μm. Bar graphs show the means ± SEM. ns, not significant. ***p < 0.001. See also Videos S9 and S10.

1195 **Data availability**

1196 RNAseq datasets have been deposited at the National Center for Biotechnology
1197 Information (NCBI) Gene Expression Omnibus (GEO) and will be publicly available as of
1198 the date of publication.

1199 Any additional information required to reanalyze the data reported in this work paper is
1200 available from the lead contact upon request.

1201

1202 **Code availability**

1203 This study did not generate original code. For *ex vivo* experiments analysis, calcium
1204 imaging code previously reported[21] has been deposited at
1205 https://github.com/ackman678/CalciumDX. For *in vivo* calcium imaging experiments, the
1206 code from WholeBrainDX repository[60] (available at
1207 https://github.com/ackman678/wholeBrainDX) was employed to prepared the
1208 supplementary videos.

1209

1210 **Tables**

1211 **Table S1. Differential expression analysis of PMBSF vs ALBSF control samples**
1212 **from bulk RNA-seq.** Related to Figures 4 and S8.

1213 **Table S2. Differential expression analysis of EmbWPC vs control-ALBSF samples**
1214 **from bulk RNA-seq.** Related to Figures 4 and S8.

1215 **Table S3. Enrichment analysis of EmbWPC and control-ALBSF samples from bulk**
1216 **RNA-seq.** Related to Figures 4 and S9.

1217

1218 **Multimedia files**

1219 **Video S1. iDISCO 3D reconstruction of E18 control mouse.** Volume of the whisker
1220 pad and upper lip areas in magenta and cyan, respectively. Volume of nice whisker pad
1221 and nine upper lip follicles in yellow. Related to Figures 1 and S1.

1222

1223 **Video S2. iDISCO 3D reconstruction of E18 embWPC mouse.** Volume of the whisker
1224 pad and upper lip areas in magenta and cyan, respectively. Volume of nice whisker pad
1225 and nine upper lip follicles in yellow. Related to Figures 1 and S1.
1226
1227 **Video S3. *In vivo* cortical evoked responses in the control side (ipsilateral to**
1228 **cauterization) of embWPC mouse at E18.** Stimulations of the whisker pad (magenta)
1229 and upper lip (cyan). Dashed lines delineate cortical hemisphere, PMBSF and ALBSF
1230 putative cortical territories. Speed x3.3. Related to Figure 2.
1231
1232 **Video S4. *In vivo* cortical evoked responses in the whisker pad cauterized (WPC)**
1233 **side (contralateral to cauterization) of embWPC mouse at E18.** Stimulations of the
1234 whisker pad (magenta) and upper lip (cyan). Dashed lines delineate cortical hemisphere,
1235 PMBSF and ALBSF putative cortical territories translated from control side stimulations
1236 ("PMBSF" and "ALBSF"). Speed x3.3. Related to Figure 2.
1237
1238 **Video S5. *In vivo* cortical evoked responses in the control side (ipsilateral to**
1239 **cauterization) of embWPC mouse at P4.** Stimulations of the whisker pad (magenta)
1240 and upper lip (cyan). Dashed lines delineate cortical hemisphere, PMBSF and ALBSF
1241 cortical territories. Speed x3.3. Related to Figure 2.
1242
1243 **Video S6. *In vivo* cortical evoked responses in the whisker pad cauterized (WPC)**
1244 **side (contralateral to cauterization) of embWPC mouse at P4.** Stimulations of the
1245 whisker pad (magenta) and upper lip (cyan). Dashed lines delineate cortical hemisphere,
1246 PMBSF and ALBSF cortical territories translated from control side stimulations
1247 ("PMBSF" and "ALBSF"). Speed x3.3. Related to Figure 2.
1248
1249 **Video S7. Spontaneous thalamic activity in the prospective VPM regions (wpVPM**
1250 **and ulVPM) in an acute slice of control mice at E16.** Dashed lines delineate dLG

1251 (dorsolateral geniculate) nucleus, prospective wpVPM and ulVPM regions. Speed x15.
1252 Related to Figure 3.
1253
1254 **Video S8. Spontaneous thalamic activity in the prospective VPM regions (wpVPM"**
1255 **and ulVPM) in an acute slice of embWPC mice at E16.** Dashed lines delineate dLG
1256 (dorsolateral geniculate) nucleus, prospective wpVPM and ulVPM regions. Speed x15.
1257 Related to Figure 3.
1258
1259 **Video S9. Topographic representations in the cortex of *in vivo* evoked responses**
1260 **in control mouse at P4.** Stimulations of the whisker pad (magenta, blue, green, yellow
1261 and orange) and upper lip (cyan and white). Dashed lines delineate cortical hemisphere,
1262 PMBSF and ALBSF evoked cortical territories. Speed x3.3. Related to Figure 6.
1263
1264 **Video S10. Topographic representations in the cortex of *in vivo* evoked responses**
1265 **in embWPC mouse at P4.** Stimulations of the upper lip (cyan and white). Dashed lines
1266 delineate cortical hemisphere and ALBSF evoked cortical territory. Speed x3.3. Related
1267 to Figure 6.

Supplemental information

A prenatal window for enhancing spatial resolution of cortical barrel maps

Mar Aníbal-Martínez, Lorenzo Puche-Aroca, Gabriele Pumo, M. Pilar Madrigal, Luis M. Rodríguez-Malmierca, Francisco J. Martini, Filippo M. Rijli, Guillermina López-Bendito

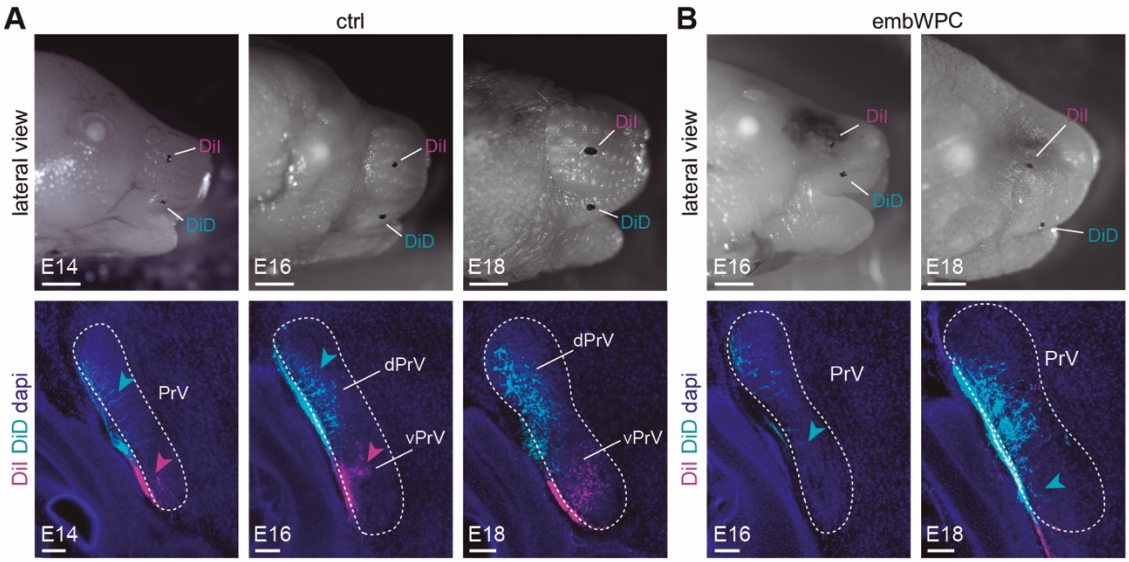

Figure S1. Early reorganization of peripheral axons at the trigeminal nucleus, Related to Figure 1. (A) Upper panels, lateral views of control mouse heads showing DiI and DiD crystal placements in the whisker pad and upper lip, respectively, at distinct developmental stages (E14, E16 and E18). Lower panels, coronal sections showing labelled axons at the vPrV (magenta, arrowheads) and dPrV (cyan, arrowheads) (n= 6 mice at E14, n= 9 mice at E16, n= 6 mice at E18). **(B)** Upper panels, lateral views of embWPC mouse heads showing DiI and DiD crystal placements in the whisker pad and upper lip, respectively, at distinct developmental stages (E16 and E18). Lower panels, coronal sections showing displaced upper lip axons at the vPrV (cyan, arrowheads) (n= 9 embWPC mice at E16, n= 5 embWPC mice at E18). E, embryonic; embWPC, embryonic whisker pad cauterized; PrV, principal nucleus; vPrV, ventral principal nucleus; dPrV, dorsal principal nucleus; DiI, 1,1′-dioctadecyl 3,3,3′,3′-tetramethylindocarbocyanine perchlorate; DiD, 1,1'-Dioctadecyl-3,3,3',3'-Tetramethylindodicarbocyanine, 4-Chlorobenzenesulfonate. Scale bars, (A, top) and (B) 1000 μm; (A, bottom) and (B) 100 μm.

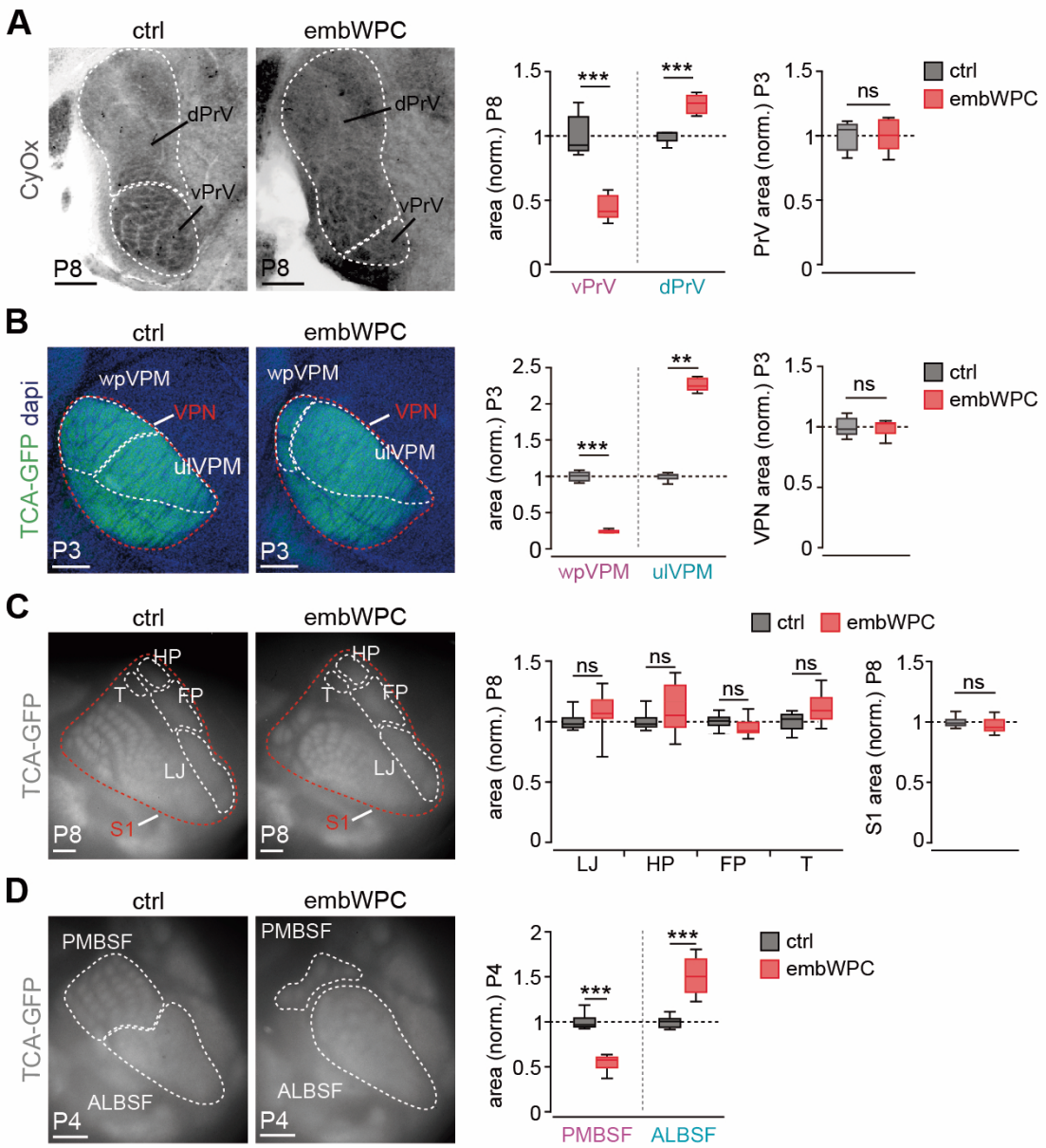

Figure S2. Intra-modal rescaling of facial whiskers representations in cortical and subcortical territories in embWPC mice. Related to Figure 1. (A) Coronal sections of the trigeminal PrV nucleus stained with CyOx in control and embWPC at P8. Quantification of the data (vPrV and dPrV areas, n= 5 ctrl mice, n= 5 embWPC mice, unpaired two-tailed Student *t*-test; PrV area, n= 5 ctrl mice, n= 5 embWPC mice, unpaired two-tailed Student *t*-test. ns, p > 0.9). **(B)** Coronal sections showing TCA-GFP labelling in the PMBSF, ALBSF and VPN of the thalamus in control and embWPC at P3. Quantification of the data (n= 5 ctrl mice, n= 5 embWPC mice, PMBSF, unpaired two-tailed Student *t*-test. ALBSF, Mann-Whitney *U*-test; VPN at P3, n= 5 ctrl mice, n= 5 embWPC mice, Mann-Whitney *U*-test. ns, p > 0.99). **(C)** Surface view of thalamocortical terminals (TCA-GFP+) in the PMBSF and ALBSF in control and embWPC mice at P8. Quantification of the data (n= 8 ctrl mice, n= 8 embWPC mice, unpaired two-tailed Student *t*-test. ns, p > 0.05. S1 area, n= 8 ctrl mice, n= 9 embWPC mice, unpaired two-tailed Student *t*-test. ns, p= 0.29). **(D)** Surface view of thalamocortical terminals (TCA-

GFP+) in the PMBSF and ALBSF in control and embWPC mice at P4. Quantification of the data (n= 6 ctrl mice, n= 6 embWPC mice, unpaired two-tailed Student *t*-test; ***$p < 0.001$). CyOx, Cytochrome oxidase; P, postnatal; wpVPM, whisker pad recipient ventral posteromedial nucleus; ulVPM, upper lip recipient ventral posteromedial nucleus; VPN, ventroposterior nucleus; TCA-GFP, thalamocortical axons labelled with green fluorescent protein; S1, primary somatosensory cortex; HP, hindpaw; FP, forepaw; LJ, lowerjaw; T, trunk; PMBSF, postero-medial barrel subfield; ALBSF, antero-lateral barrel subfield; norm., normalized. Scale bars, (A) and (B) 200 μm; (C) and (D) 500 μm. Boxplots show the medians with the interquartile range (box) and range (whiskers). ns, not significant. **$p < 0.01$, ***$p < 0.001$.

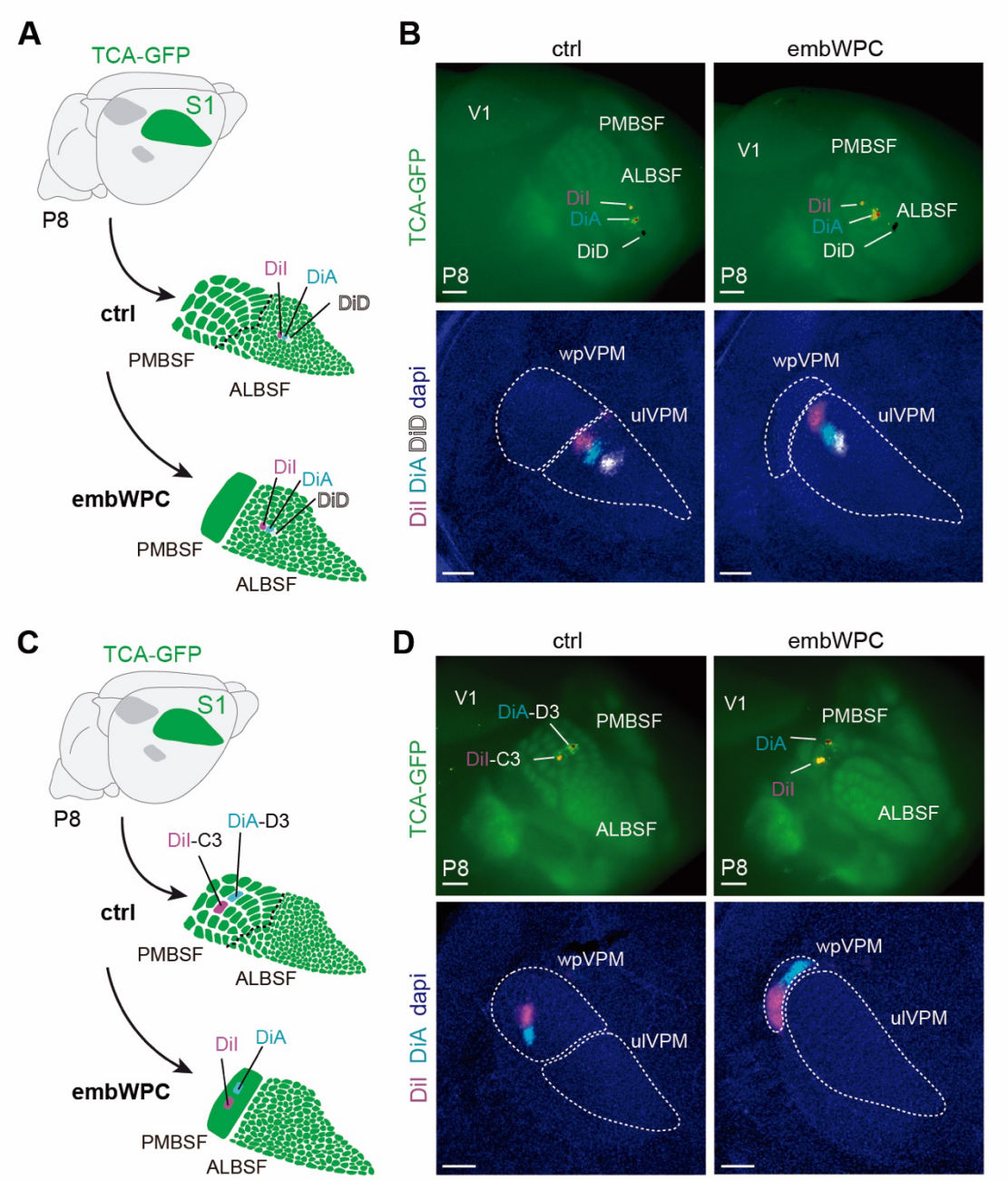

Figure S3. Thalamocortical point-to-point topography in embWPC mice. Related to Figure 1. (A) Schema representing the experimental paradigm. **(B)** Upper panels, DiI, DiA and DiD crystal placements subsequent non-overlapping points in the ALBSF in control and embWPC at P8. Lower panels, backlabelled cells at the ulVPM showed a shifted relative displacement toward the wpVPM in embWPC mice (n= 8 ctrl mice, n= 8 embWPC mice). **(C)** Schema representing the experimental paradigm. **(D)** Upper panels, DiI and DiA crystal placements in the C3 and D3 cortical barrels, respectively, in PMBSF control and in the remaining territory of the PMBSF in embWPC at P8. Lower panels, backlabelled cells maintain their point-to-point distribution at the wpVPM both in control and embWPC mice (n= 9 ctrl mice, n= 9 embWPC mice). V1, primary visual cortex; DiA, 4-[4-(dihexadecylamino) styryl]-N-methylpyridinium iodide. Scale bars, (B and D, top) 500 μm; (B and D, bottom) 200 μm.

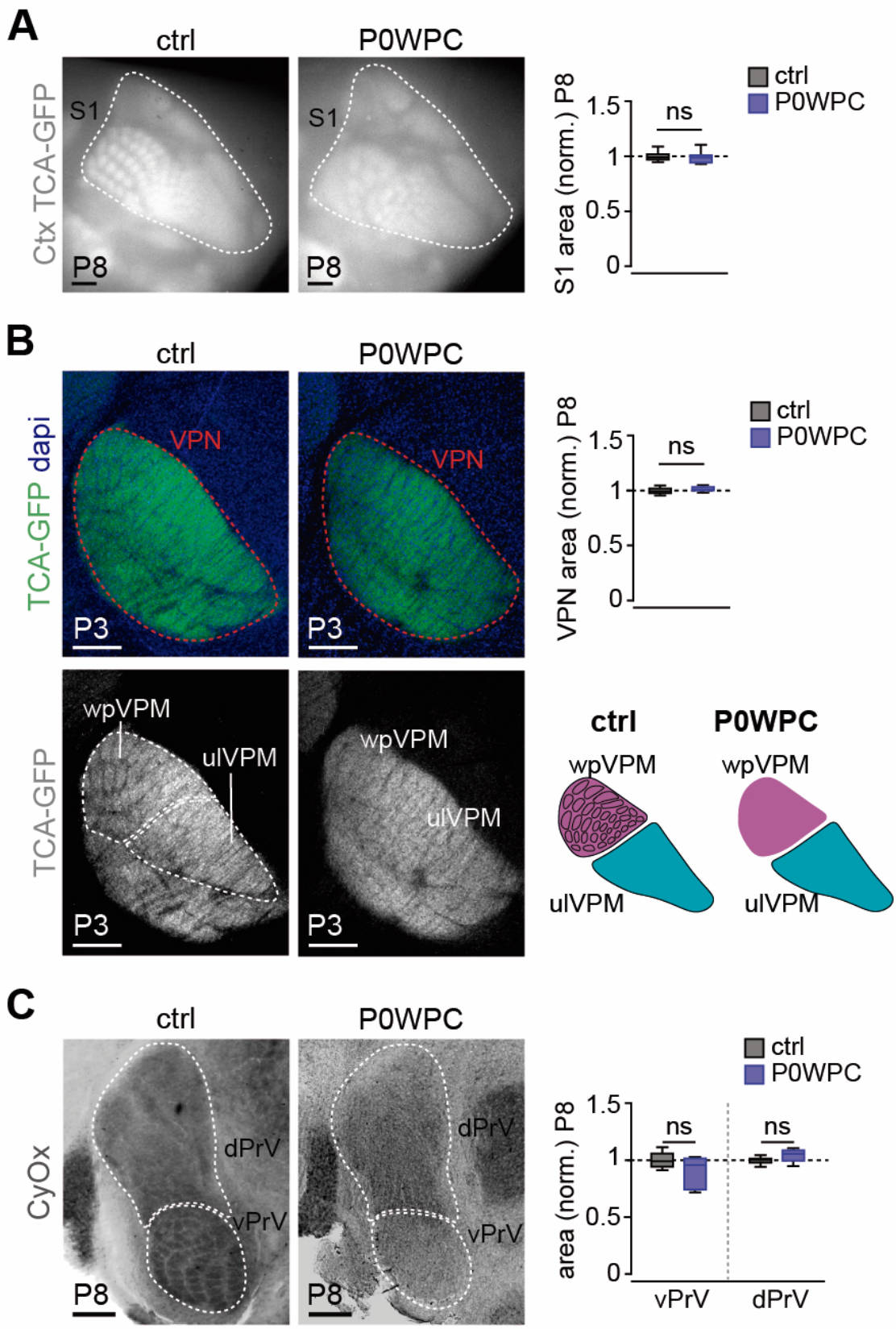

Figure S4. Cortical and subcortical areas for facial whiskers representations remained unchanged in P0WPC mice. Related to Figure 1. (A) Surface view of thalamocortical terminals (TCA-GFP+) in the cortical S1 in control and P0WPC mice at

P8. Quantification of the total S1 area (n= 8 ctrl mice, n= 9 P0WPC mice, unpaired two-tailed Student *t*-test. ns, p= 0.66). **(B)** Coronal sections showing TCA-GFP labelling in the PMBSF, ALBSF and VPN of the thalamus in control and P0WPC at P3. Quantification of the VPN area and schema representing the results (n= 8 ctrl mice, n= 9 P0WPC mice, unpaired two-tailed Student *t*-test. ns, p= 0.39). **(C)** Coronal sections of the trigeminal PrV nucleus stained with CyOx in control and P0WPC at P8. Quantification of the vPrV and dPrV area (n= 5 ctrl mice, n= 5 P0WPC mice, unpaired two-tailed Student *t*-test. ns, p> 0.20). P0WPC, postnatal day 0 whisker pad cauterized. Scale bars, (A) 500 μm; (B) and (C) 200 μm. Boxplots show the medians with the interquartile range (box) and range (whiskers). ns, not significant.

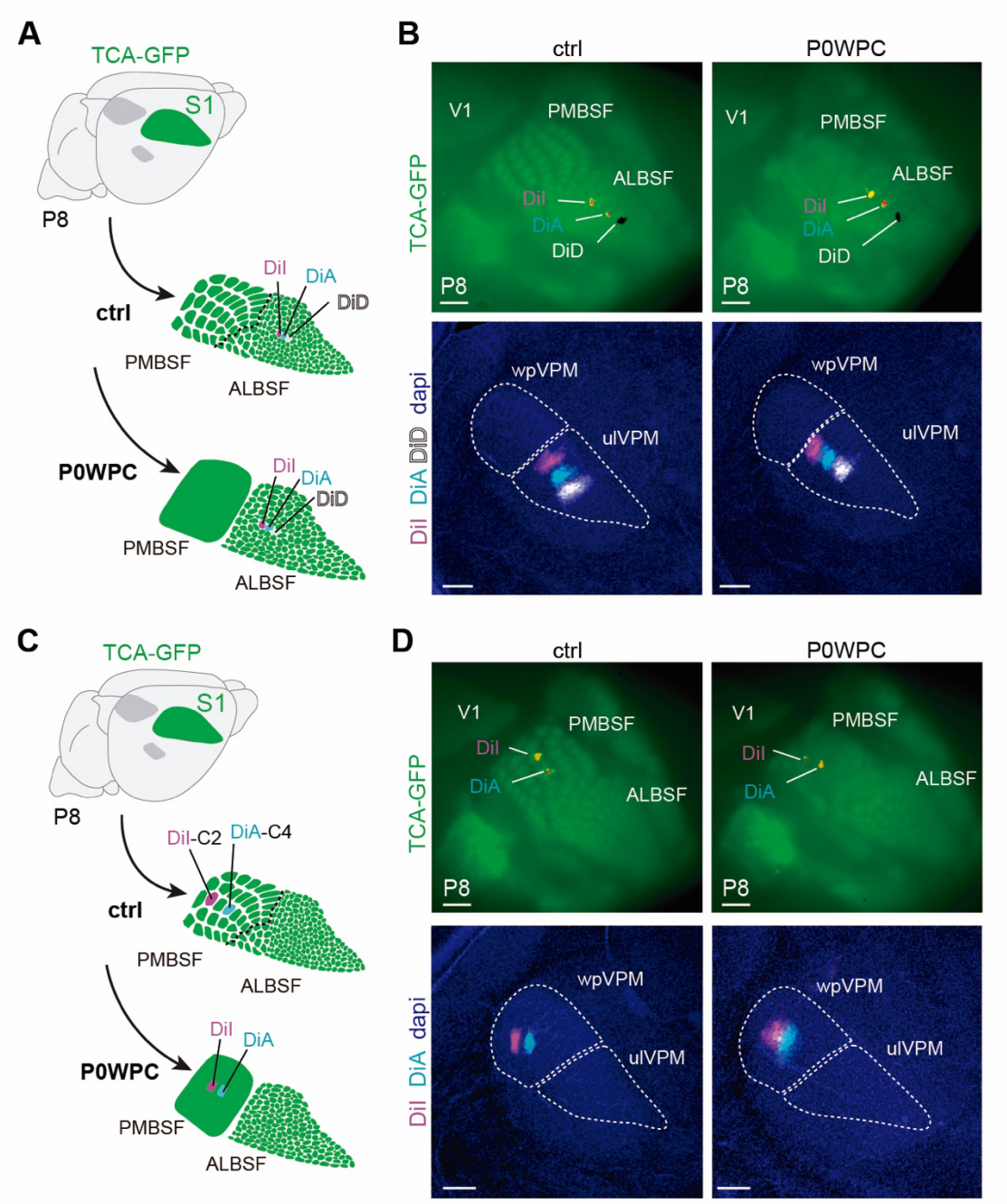

Figure S5. Thalamocortical point-to-point topography in P0WPC mice. Related to Figure 1. (A) Schema representing the experimental paradigm. **(B)** Upper panels, DiI, DiA and DiD crystal placements subsequent non-overlapping positions in the ALBSF in control and P0WPC at P8. Lower panels, backlabelled cells at the ulVPM (n= 7 ctrl mice, n= 7 P0WPC mice). **(C)** Schema representing the experimental paradigm. **(D)** Upper panels, DiI and DiA crystal placements in the C2 and C4 cortical barrels, respectively, in control and in the deprived PMBSF territory in P0WPC at P8. Lower panels, backlabelled cells showing their point-to-point distribution at the wpVPM in control and P0WPC mice (n= 7 ctrl mice, n= 7 P0WPC mice). Scale bars, (B and D, top) 500 μm; (B and D, bottom) 200 μm.

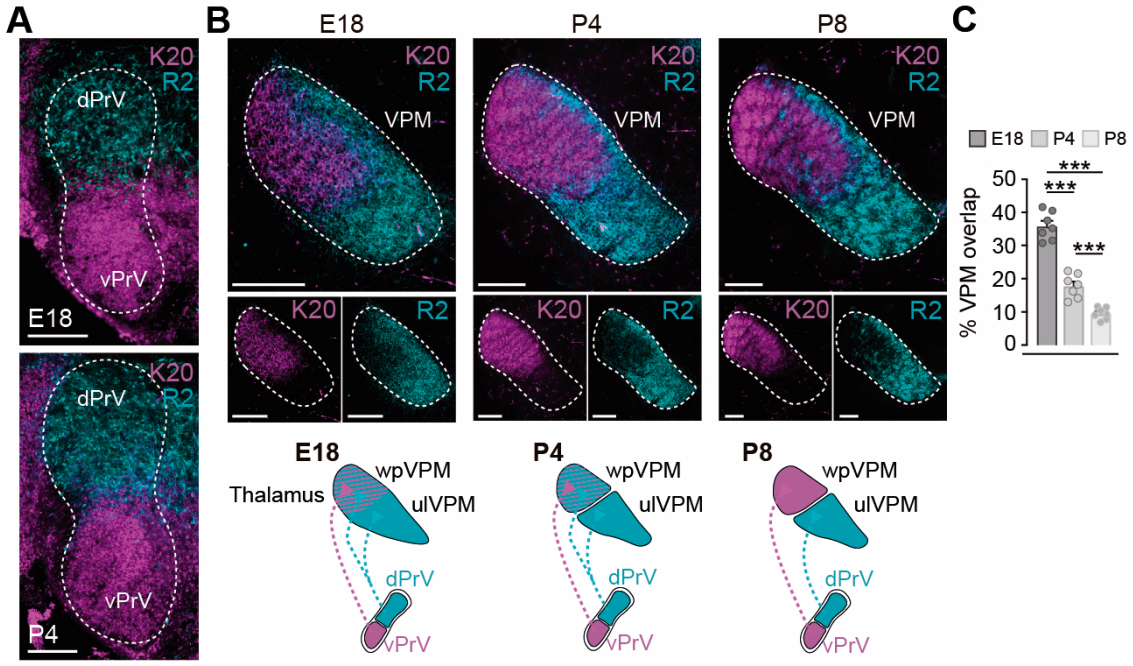

Figure S6. Developmental progression of trigemino-thalamic axons. Related to Figure 3. (A) Coronal sections from the *Krox20-zsgreen::R2-mCherry* double transgenic mouse showing cells expressing Krox20 (magenta) at the vPrV and R2 (cyan) at the dPrV at E18 and P4 (n= 7 E18, n= 7 P4). **(B)** Coronal sections from the *Krox20-zsgreen::R2-mCherry* double transgenic mice showing Krox20-labelled axons (magenta) and R2-labelled axons (cyan) at the VPM of the thalamus at E18, P4 and P8. Schemas representing the results found. **(C)** Quantification of the percentage of developmental overlap between vPrV and dPrV axons at the thalamus (n= 7 E18, n= 7 P4, n= 8 P8, Two-way ANOVA test: ***p <0.001. Tukey's multiple comparison test *post-hoc* analysis). Scale bars, 200 μm**.** Bar graphs show the means ± SEM. ***p <0.001.

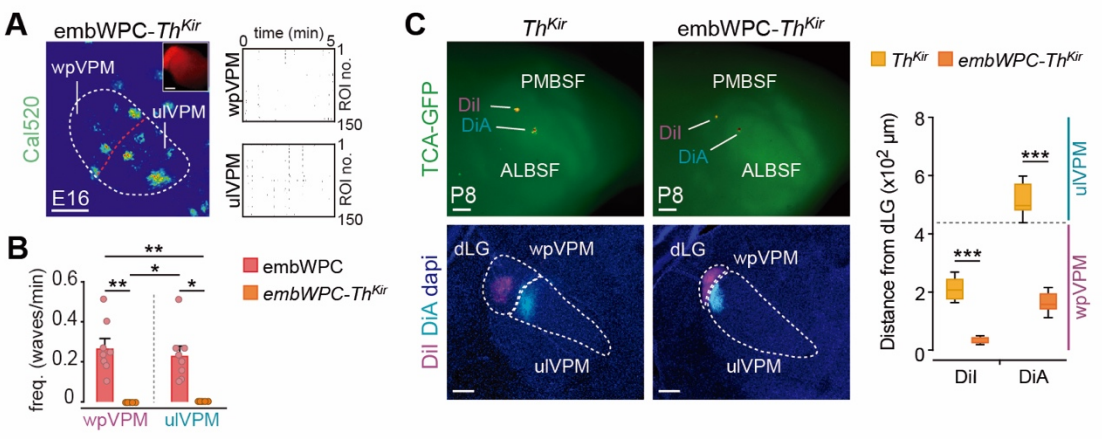

Figure S7. Thalamocortical point-to-point topography is shifted in embWPC-*Th*^{Kir} but not in *Th*^{Kir} mouse. Related to Figure 3. (A) Maximal projection of *ex vivo* spontaneous calcium activity in the prospective VPM sub-regions (wpVPM, wp input-receiving neurons, and ulVPM, ul input-receiving neurons) of the thalamus in acute slices at E16. Raster plots of 5 minutes. **(B)** Quantification of the frequency of waves activity in the VPM in both embWPC and embWPC-*Th*^{Kir} mice (n= 8 embWPC mice, n= 5 embWPC-*Th*^{Kir} mice, Kruskal-Wallis test, ***p <0.001. Dunn's multiple comparison test post-hoc analysis). **(C)** Upper panels, DiI and DiA crystal placements in the cortical PMBSF and ALBSF areas, respectively. Lower panels, backlabelled cells at the thalamus show shifted positions within the ALBSF thalamic area in the embWPC-*Th*^{Kir} mice as compared to *Th*^{Kir} at P8. Quantification of the position of backlabelled cells with respect to the distance to the dLG nucleus. The gray horizontal dashed line in the graph represents the separation between PMBSF and ALBSF (n= 6 *Th*^{Kir} mice, n= 6 embWPC-*Th*^{Kir} mice, unpaired two-tailed Student *t*-test). Scale bars, (A) and (C, bottom) 200 µm; (C, top) 500 µm. Bar graphs show the means ± SEM. *p < 0.05, **p < 0.01, ***p < 0.001.

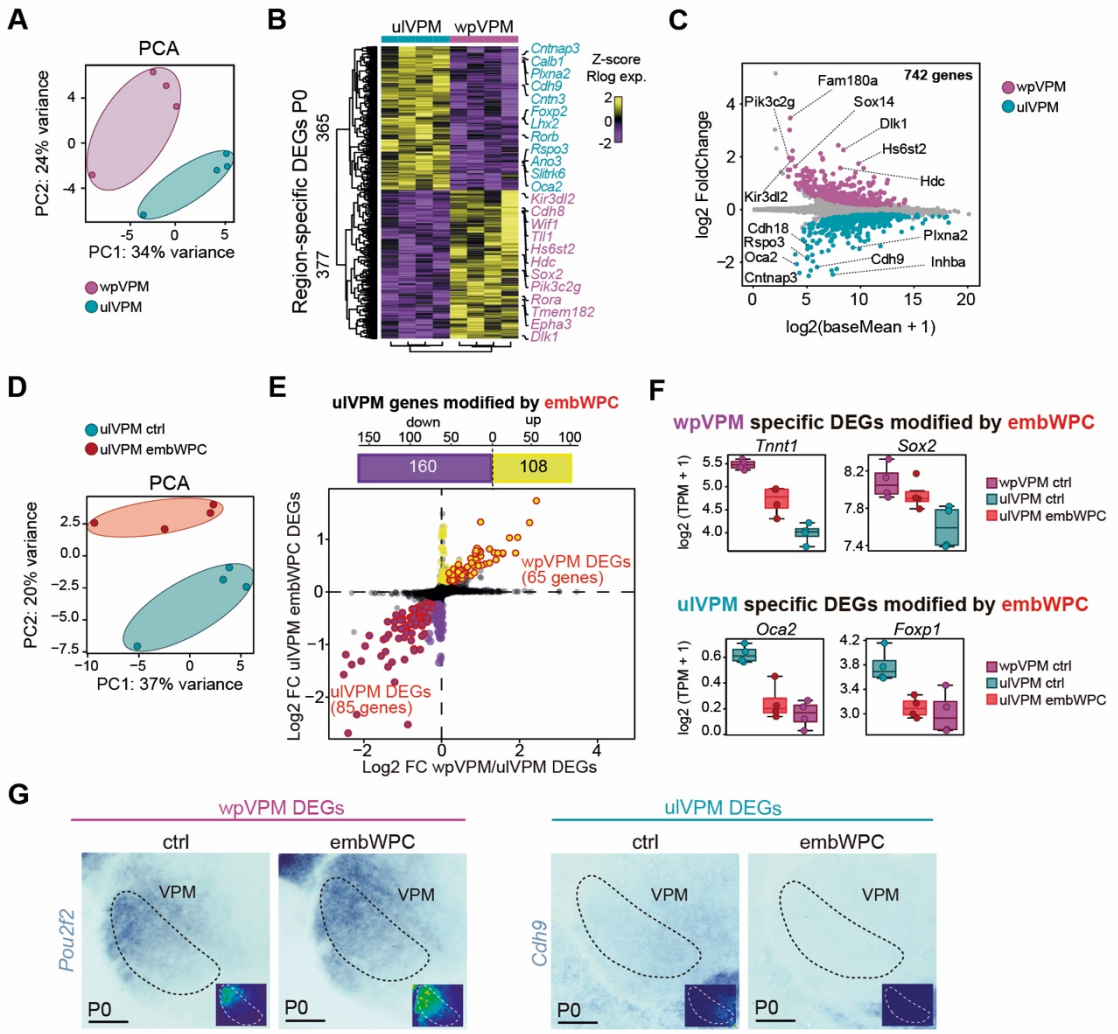

Figure S8. Region-specific transcriptional signatures in the thalamic VPM sub-regions in control and embWPC mice at P0. Related to Figure 4. (A) Principal Component Analysis (PCA) of wpVPM (n= 4) and ulVPM (n= 4) control mice at P0. **(B)** Heatmap of normalized regularized logarithm (Rlog) Z-score of expression and unbiased clustering of ulVPM- and wpVPM-specific Differentially Expressed Genes (DEGs) at P0. The color-code (yellow, high expression; purple, low expression) corresponds to the log2FC. **(C)** MA plot showing the log2 FoldChange and the mean expression distribution of DEGs. The magenta and cyan dots represent wpVPM and ulVPM DEGs, respectively, with the top 7 protein coding genes listed in every region. **(D)** Principal Component Analysis (PCA) of thalamic control ulVPM (n= 4) and embWPC ulVPM (n= 4) mice at P0. **(E)** Top, histogram showing ulVPM DEGs that are up- and downregulated by embWPC at P0. Bottom, scatterplot of log2Foldchange between ulVPM DEGs modified by embWPC and wpVPM versus ulVPM region-specific DEGs. **(F)** Boxplots displaying TPM expression levels of selected wpVPM DEGs and ulVPM DEGs modified in the ulVPM of the embWPC mice. Boxplots show the medians with the interquartile range (box) and range (whiskers). **(G)** Coronal sections showing by in situ hybridization the change in the pattern of expression of additional wpVPM and ulVPM DEGs in the embWPC mouse at P0 (n= 5 ctrl, n= 5 embWPC, for each probe). Scale bars, 200 μm.

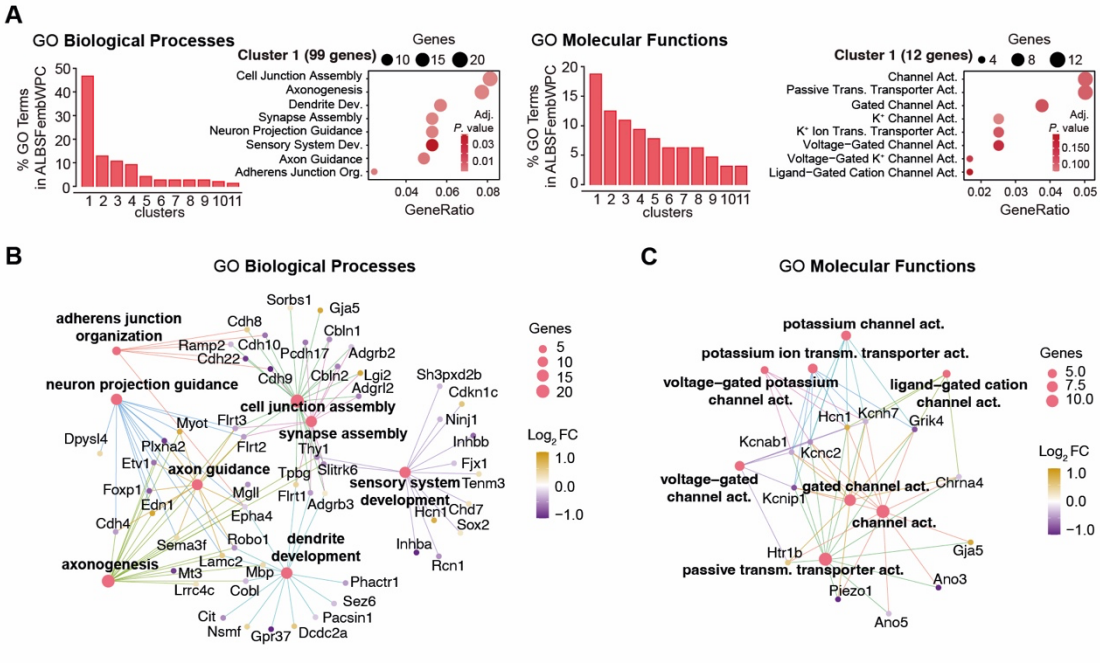

Figure S9. Gene Ontology analysis of region-specific genes modified in embWPC mice. Related to Figure 4. (A) Gene Ontology (GO) functional analysis (Biological Processes, left; and Molecular Functions, right) showing the top ranked clusters of GO terms enriched in the region-specific gene-set modified in embWPC-ulVPM. **(B)** Gene ontology (GO) biological process (BP) enrichment analysis of wpVPM and ulVPM DEGs modified by embWPC in ulVPM. **(C)** Gene ontology (GO) molecular function (MF) enrichment analysis of wpVPM and ulVPM DEGs modified by embWPC in ulVPM. The size of every node (enriched term) in the gene networks represents the number of genes enriched and the color-code (yellow, high expression; purple, low expression) corresponds to the log2FC in the wpVPM vs ulVPM Differential expression analysis (DEA).

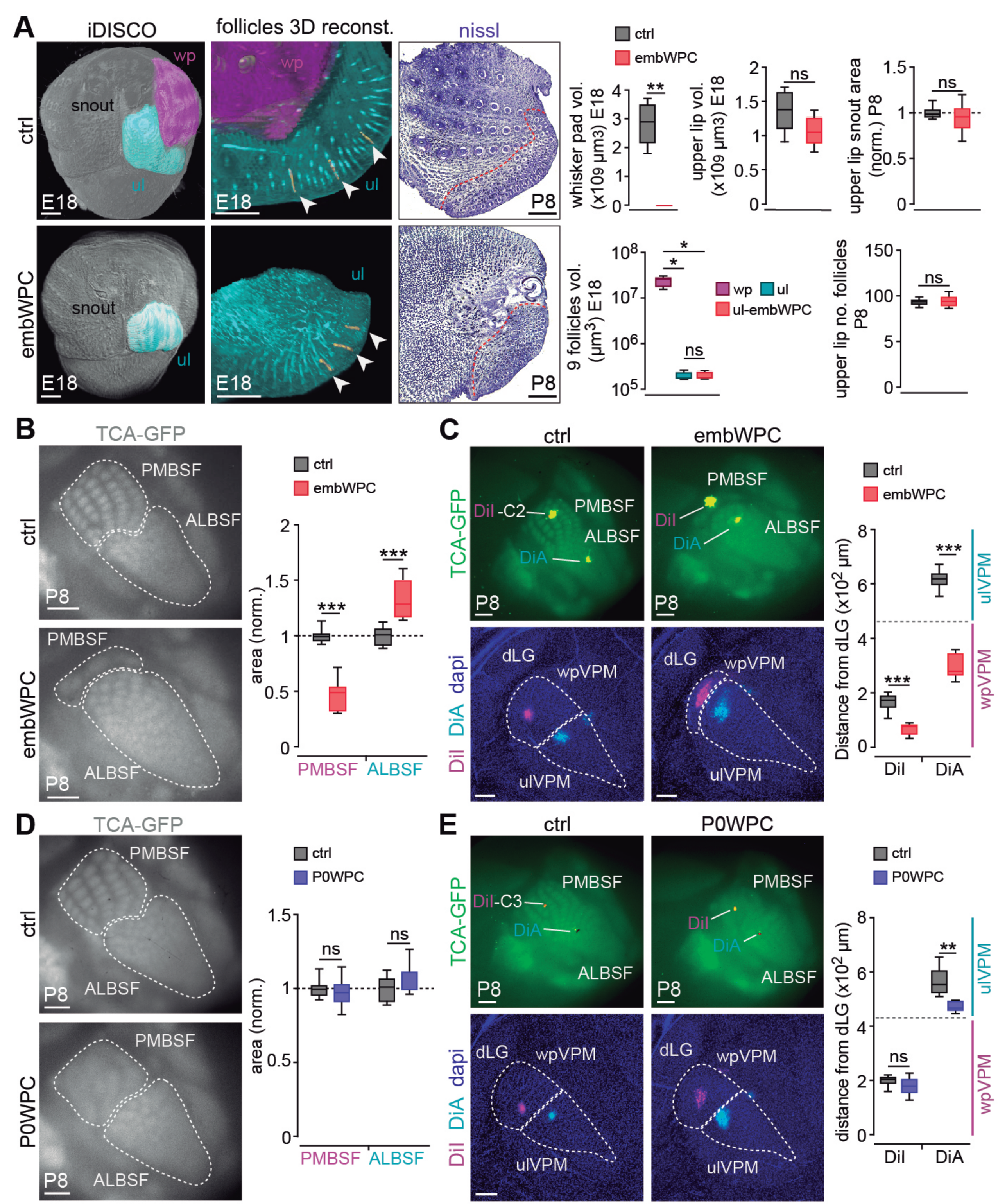
A
iDISCO
follicles 3D reconst.
nissl
ctrl
embWPC
wp
snout
ul
E18
P8
ctrl
embWPC
whisker pad vol. (x10⁹ µm3) E18
upper lip vol. (x10⁹ µm3) E18
upper lip snout area (norm.) P8
ns
**
9 follicles vol. (µm³) E18
wp
ul
ul-embWPC
*
ns
upper lip no. follicles P8
B
TCA-GFP
PMBSF
ALBSF
area (norm.)
***
C
DiI -C2
DiA
dLG
wpVPM
ulVPM
DiI DiA dapi
Distance from dLG (x10² µm)
DiI
DiA
D
P0WPC
E
distance from dLG (x10² µm)
**

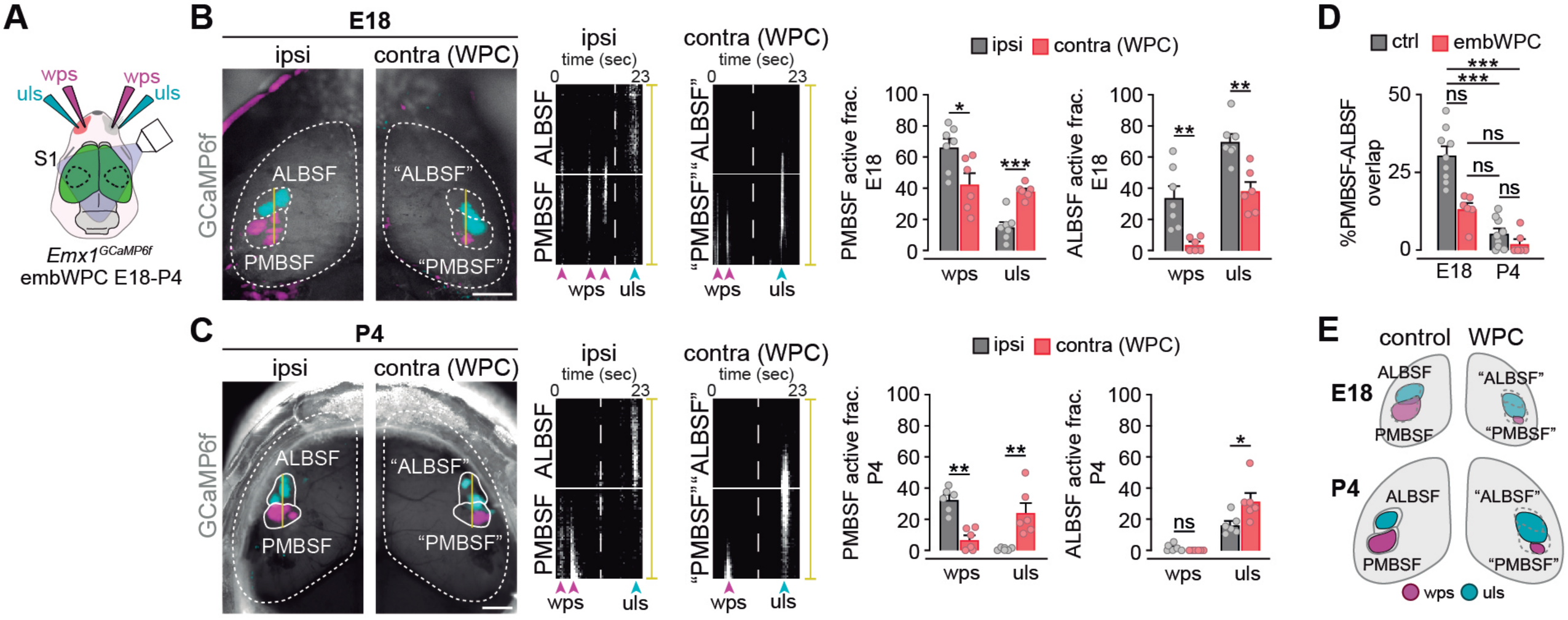
A
wps
uls
wps
uls
S1
Emx1GCaMP6f
embWPC E18-P4
B
E18
ipsi
contra (WPC)
GCaMP6f
ALBSF
PMBSF
"ALBSF"
"PMBSF"
ipsi
time (sec)
0
23
ALBSF
PMBSF
wps
uls
contra (WPC)
time (sec)
0
23
"PMBSF"
"ALBSF"
wps
uls
ipsi
contra (WPC)
PMBSF active frac. E18
100
80
60
40
20
0
*
***
wps
uls
ALBSF active frac. E18
**
**
wps
uls
C
P4
ipsi
contra (WPC)
GCaMP6f
ALBSF
PMBSF
"ALBSF"
"PMBSF"
ipsi
time (sec)
0
23
ALBSF
PMBSF
wps
uls
contra (WPC)
time (sec)
0
23
"PMBSF"
"ALBSF"
wps
uls
ipsi
contra (WPC)
PMBSF active frac. P4
**
**
wps
uls
ALBSF active frac. P4
ns
*
wps
uls
D
ctrl
embWPC
%PMBSF-ALBSF overlap
50
25
0
***
***
ns
ns
ns
ns
E18
P4
E
control
WPC
E18
ALBSF
PMBSF
"ALBSF"
"PMBSF"
P4
ALBSF
PMBSF
"ALBSF"
"PMBSF"
wps
uls

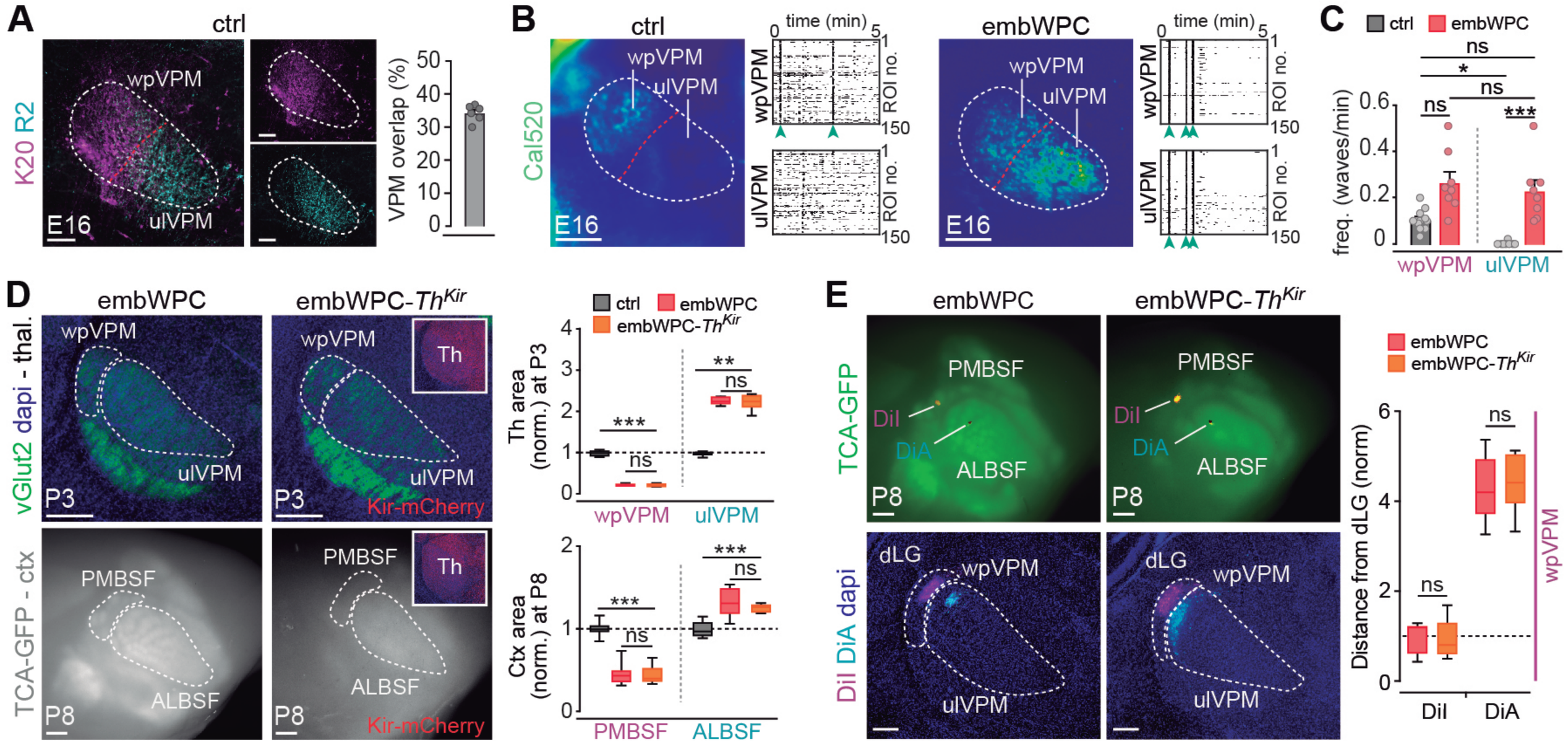
A
ctrl
K20 R2
wpVPM
ulVPM
E16
VPM overlap (%)
50
40
30
20
10
0
B
ctrl
Cal520
wpVPM
ulVPM
E16
time (min)
0
5
ROI no.
1
150
embWPC
C
ctrl
embWPC
ns
*
ns
ns
***
freq. (waves/min)
0.6
0.4
0.2
0
wpVPM
ulVPM
D
embWPC
embWPC-ThKir
vGlut2 dapi - thal.
Th
Kir-mCherry
P3
TCA-GFP - ctx
PMBSF
ALBSF
P8
Th area (norm.) at P3
Ctx area (norm.) at P8
**
***
ns
E
TCA-GFP
DiI
DiA
DiI DiA dapi
dLG
Distance from dLG (norm)
6
4
2
0

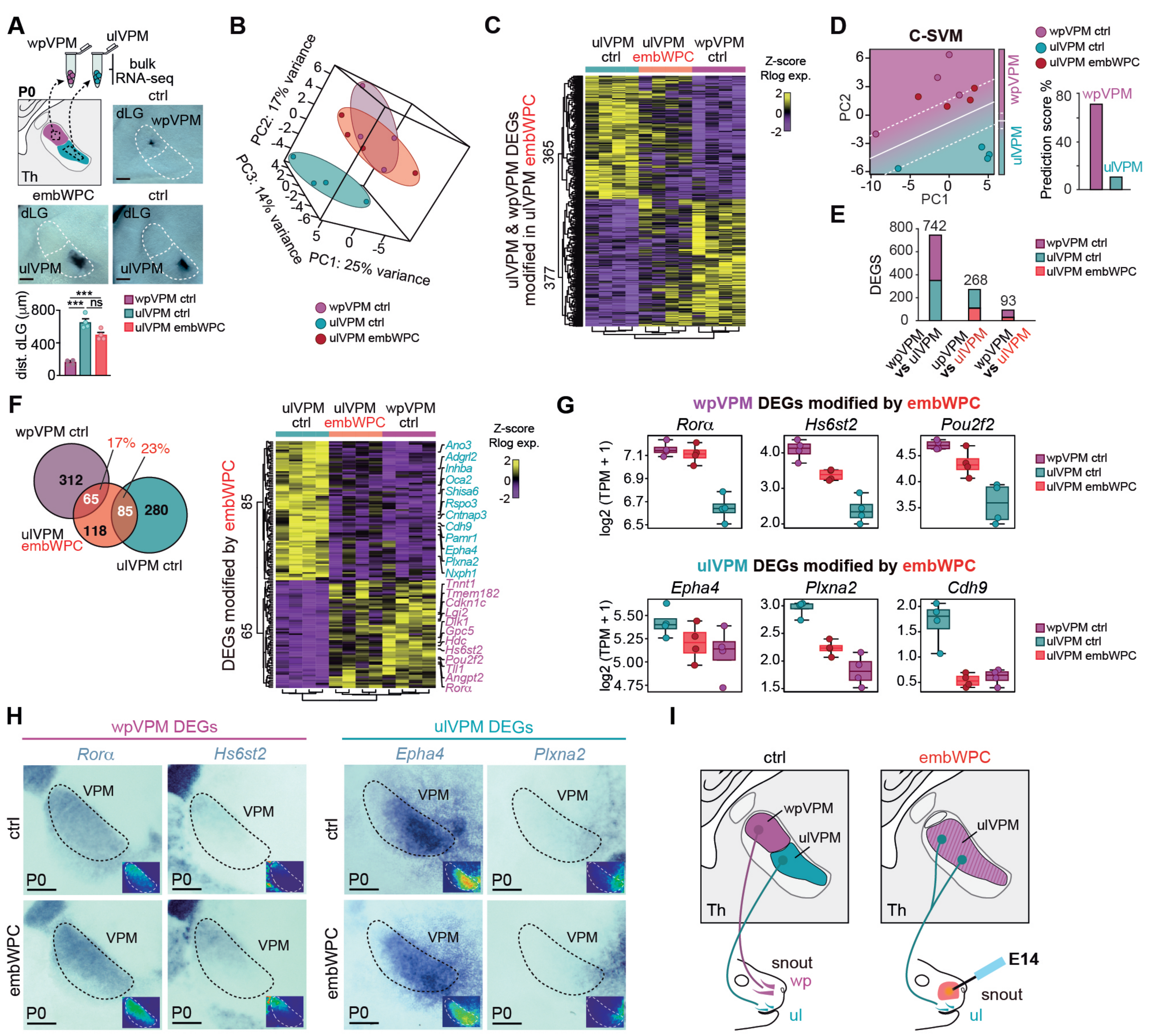
A
wpVPM
ulVPM
bulk RNA-seq
P0
ctrl
dLG
wpVPM
Th
embWPC
ctrl
dLG
dLG
ulVPM
ulVPM
dist. dLG (µm)
800
400
0
***
***
ns
wpVPM ctrl
ulVPM ctrl
ulVPM embWPC
B
PC2: 17% variance
PC3: 14% variance
PC1: 25% variance
wpVPM ctrl
ulVPM ctrl
ulVPM embWPC
C
ulVPM ctrl
ulVPM embWPC
wpVPM ctrl
Z-score Rlog exp.
ulVPM & wpVPM DEGs modified in ulVPM embWPC
365
377
D
C-SVM
PC2
PC1
wpVPM
ulVPM
wpVPM ctrl
ulVPM ctrl
ulVPM embWPC
Prediction score %
wpVPM
ulVPM
E
DEGS
742
268
93
wpVPM vs ulVPM
upVPM vs ulVPM
wpVPM vs ulVPM
wpVPM ctrl
ulVPM ctrl
ulVPM embWPC
F
wpVPM ctrl
17%
23%
312
65
85
280
118
ulVPM embWPC
ulVPM ctrl
ulVPM ctrl
ulVPM embWPC
wpVPM ctrl
Z-score Rlog exp.
DEGs modified by embWPC
85
65
Ano3
Adgrl2
Inhba
Oca2
Shisa6
Rspo3
Cntnap3
Cdh9
Pamr1
Epha4
Plxna2
Nxph1
Tnnt1
Tmem182
Cdkn1c
Lgi2
Dlk1
Gpc5
Hdc
Hs6st2
Pou2f2
Tll1
Angpt2
Rorα
G
wpVPM DEGs modified by embWPC
Rorα
Hs6st2
Pou2f2
log2 (TPM + 1)
wpVPM ctrl
ulVPM ctrl
ulVPM embWPC
ulVPM DEGs modified by embWPC
Epha4
Plxna2
Cdh9
log2 (TPM + 1)
wpVPM ctrl
ulVPM ctrl
ulVPM embWPC
H
wpVPM DEGs
ulVPM DEGs
Rorα
Hs6st2
Epha4
Plxna2
ctrl
embWPC
VPM
P0
I
ctrl
embWPC
wpVPM
ulVPM
Th
snout
wp
ul
E14
snout
ul

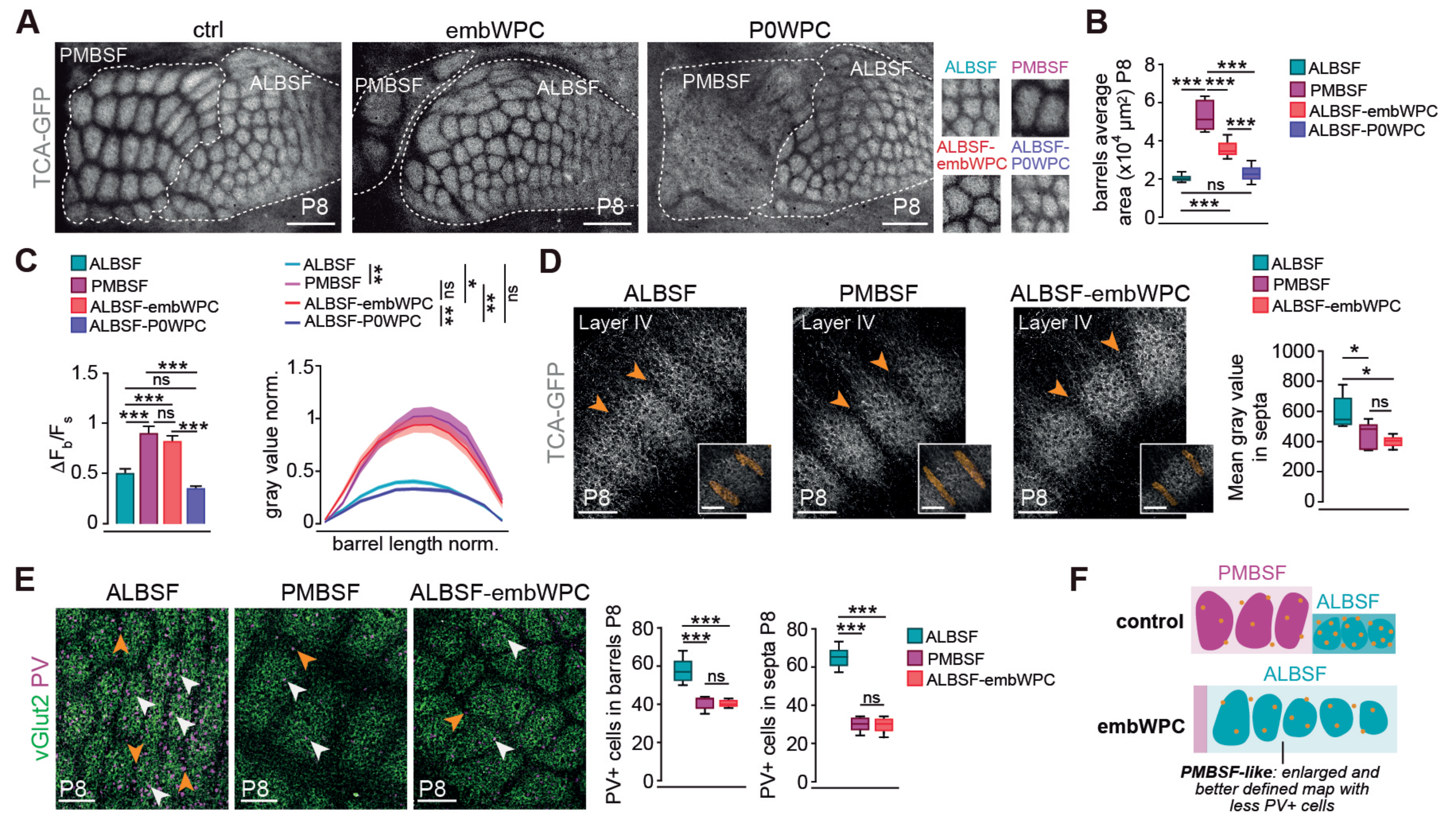
A
ctrl
embWPC
P0WPC
TCA-GFP
PMBSF
ALBSF
P8
ALBSF
PMBSF
ALBSF-embWPC
ALBSF-P0WPC
B
barrels average area (x10⁴ µm²) P8
ALBSF
PMBSF
ALBSF-embWPC
ALBSF-P0WPC
C
ΔF_b/F_s
gray value norm.
barrel length norm.
D
ALBSF
PMBSF
ALBSF-embWPC
Layer IV
Mean gray value in septa
E
vGlut2 PV
PV+ cells in barrels P8
PV+ cells in septa P8
F
control
embWPC
PMBSF-like: enlarged and better defined map with less PV+ cells

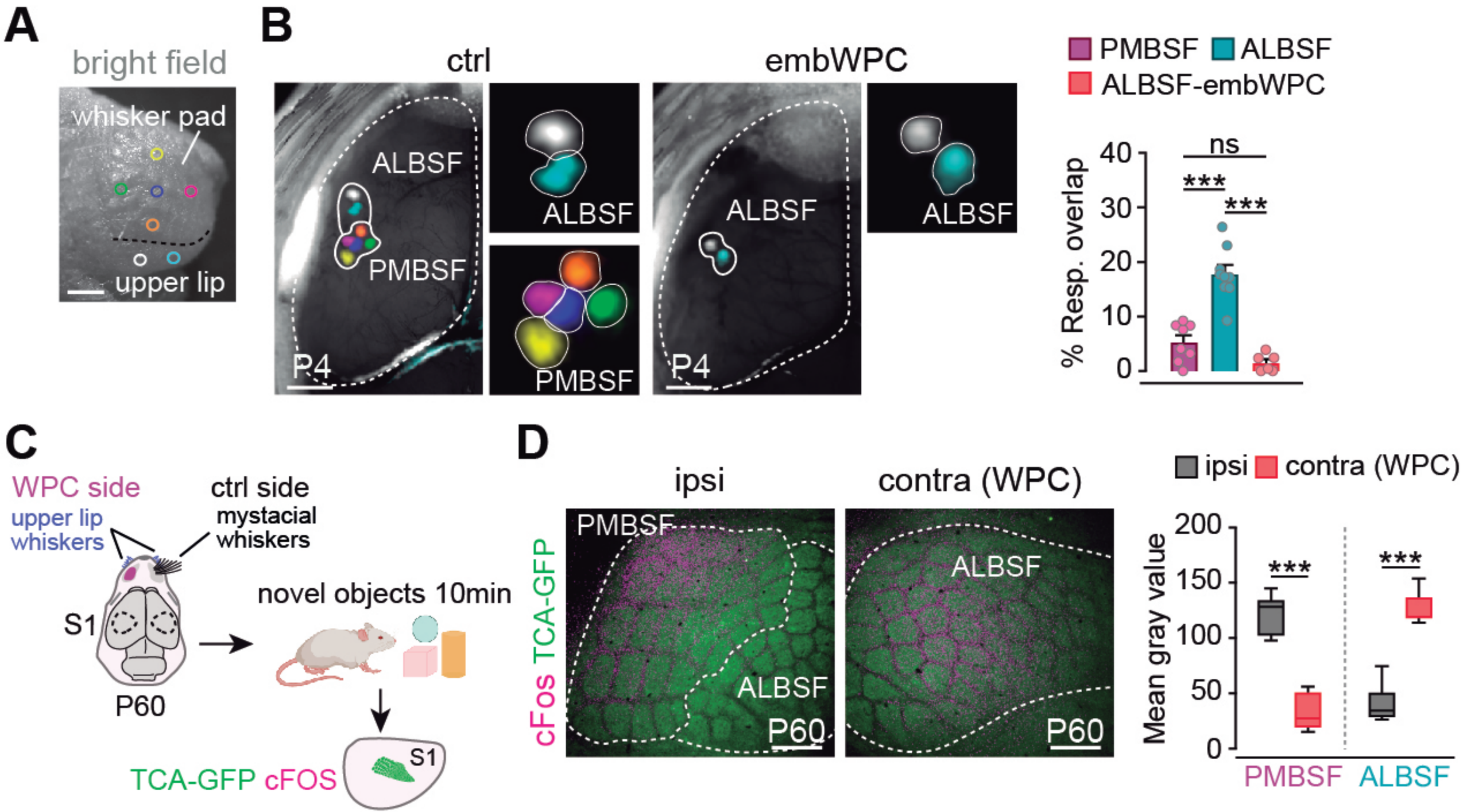
A
bright field
whisker pad
upper lip
B
ctrl
embWPC
ALBSF
PMBSF
P4
ALBSF
PMBSF
ALBSF
P4
ALBSF
PMBSF
ALBSF-embWPC
% Resp. overlap
40
30
20
10
0
ns
***
***
C
WPC side
upper lip
whiskers
ctrl side
mystacial
whiskers
S1
P60
novel objects 10min
TCA-GFP cFOS
S1
D
ipsi
contra (WPC)
cFos TCA-GFP
PMBSF
ALBSF
P60
ALBSF
P60
ipsi
contra (WPC)
Mean gray value
200
150
100
50
0
***
***
PMBSF
ALBSF